AFRL-OSR-VA-TR-2015-0089

(STTR PHII) Reactive Fusion Welding for Ultra-High Temperature

Cheol-Woon Kim
MO SCI CORP

03/16/2015
Final Report

Air Force Research Laboratory
AF Office Of Scientific Research (AFOSR)/ RTD
Arlington, Virginia 22203
Air Force Materiel Command

REPORT DOCUMENTATION PAGE	*Form Approved* *OMB No. 0704-0188*

1. REPORT DATE *(DD-MM-YYYY)* 13-03-2015	**2. REPORT TYPE** STTR Phase II Final Technical	**3. DATES COVERED** *(From - To)* 15 Mar 2012 – 14 Dec 2014
4. TITLE AND SUBTITLE Reactive Fusion Welding for Ultra-High Temperature Ceramic Composite Joining		**5a. CONTRACT NUMBER** FA9550-12-C-0060
		5b. GRANT NUMBER
		5c. PROGRAM ELEMENT NUMBER
6. AUTHOR(S) Cheol-Woon Kim (MO-SCI Corporation); Derek S. King, Gregory E. Hilmas, and William G. Fahrenholtz (Missouri University of Science & Technology)		**5d. PROJECT NUMBER**
		5e. TASK NUMBER
		5f. WORK UNIT NUMBER
7. PERFORMING ORGANIZATION NAME(S) AND ADDRESS(ES) MO-SCI Corporation, 4040 Hy Point North, Rolla, MO 65401; Missouri University of Science & Technology, 1400 N. Bishop Ave., Rolla, MO 65409		**8. PERFORMING ORGANIZATION REPORT NUMBER**
9. SPONSORING / MONITORING AGENCY NAME(S) AND ADDRESS(ES) Air Force Office of Scientific Research, 875 N. Randolph St., Room 3112, Arlington, VA 22203		**10. SPONSOR/MONITOR'S ACRONYM(S)**
		11. SPONSOR/MONITOR'S REPORT NUMBER(S)

12. DISTRIBUTION / AVAILABILITY STATEMENT
Approved for public release; distribution unlimited

13. SUPPLEMENTARY NOTES

14. ABSTRACT

Plasma and pulsed plasma arc welding (PAW and PPAW) processes were used to fusion weld ZrB_2 containing 20 vol% ZrC. Varying welding parameters resulted in changes in weld pool shape and size, and the size of ZrB_2 grains within the fusion zone (FZ). For PAW processes that resulted in a keyhole fusion zone (full penetration), the arc to workpiece power transfer efficiency was estimated to be <24%. Power transfer efficiency was estimated to drop to <18% for non-keyhole welds. The power transfer efficiency was not estimated for PPAW processes, but keyhole formation was observed for PPAW FZs. ZrB_2 grain lengths were observed to decrease between binary PAW FZs (~1 mm in length), and binary PPAW FZs (~0.8 mm in length), and an increasing aspect ratio for ZrB_2 grains in PPAW welds (up to 40:1) compared to PAW ZrB_2 grain aspect ratios (up to 25:1) revealed that growth of ZrB_2 was hindered in PPAW FZs. Grain growth was also observed to decrease with decreasing arc power. A high arc power resulted in high growth rates of ZrB_2 and a textured FZ, whereas lower arc power FZs did not exhibit texture. A high current plasma arc (222 A) was used to increase the temperature of the weld pool, such that ZrB_2 growth would follow the arc thermal gradient. ZrB_2 growth occurred in the basal plane, resulting in grains with a plate-like morphology, where grain thickness increased by ledge growth. ZrB_2 grain sizes within the FZ were observed to affect the strength of weldments. PM flexure strengths were measured to be ~660 MPa and strengths were observed to drop to ~140 MPa for PAW weldments and ~170 MPa for PPAW weldments. Diffusion of C into the melt pool was observed to hinder ZrB_2 grain growth significantly (~150 μm maximum ZrB_2 grain size). The decreased maximum grain size resulted in average flexure strength of ~250 MPa for ZrB_2-ZrC-C weldments.

15. SUBJECT TERMS
STTR report, fusion welding, joining, ceramics

16. SECURITY CLASSIFICATION OF:			**17. LIMITATION OF ABSTRACT**	**18. NUMBER OF PAGES**	**19a. NAME OF RESPONSIBLE PERSON** Cheol-Woon Kim
a. REPORT Unclassified	**b. ABSTRACT** Unclassified	**c. THIS PAGE** Unclassified			**19b. TELEPHONE NUMBER** *(include area code)* 573-364-2338

TABLE OF CONTENTS

1.0 ABSTRACT 1
2.0 INTRODUCTION 2
3.0 EXPERIMENTAL PROCEDURES 3
3.1 Powder Processing 3
3.2 Welding 4
3.3 Machining and Mechanical Testing 6
3.4 Microscopy 7
4.0 RESULTS AND DISCUSSION 7
4.1 Fusion Welding of UHTCs 7
4.1.1 ZrB_2-ZrC Welding 7
4.1.2 TiB_2-TiC Welding 15
4.1.3 ZrB_2-ZrC-WC Welding 17
4.1.4 ZrC-TiC Welding 19
4.1.5 W Filler Material 20
4.1.6 TiB_2-TiC-B_4C GTAW 21
4.1.7 Applications for Welding UHTCs 23
4.2 Mechanical Properties 27
4.2.1 Parent Material Mechanical Properties 27
4.2.2 Welded ZrB_2-20ZrC Flexure Strengths 29
4.3 Melt Solidification 33
4.3.1 ZrB_2 Growth 41
4.3.2 ZrC Precipitation 43
4.4 Plasma Jet Testing 45
5.0 SUMMARY AND CONCLUSIONS 49
6.0 RECOMMENDATIONS FOR FUTURE WORK 51
7.0 REFERENCES 54
APPENDIX A-Personnel and Publications 57
APPENDIX B-Presentations/Posters and Abstracts 58
2013 58
2014 60

2015 65
LIST OF ACRONYMS AND DESIGNATIONS 66

1.0 ABSTRACT

Plasma and pulsed plasma arc welding (PAW and PPAW) processes were used to fusion weld ZrB_2 containing 20 vol% ZrC. Varying welding parameters resulted in changes in weld pool shape and size, and the size of ZrB_2 grains within the fusion zone (FZ). For PAW processes that resulted in a keyhole fusion zone (full penetration), the arc to workpiece power transfer efficiency was estimated to be <24%. Power transfer efficiency was estimated to drop to <18% for non-keyhole welds. The power transfer efficiency was not estimated for PPAW processes, but keyhole formation was observed for PPAW FZs. ZrB_2 grain lengths were observed to decrease between binary PAW FZs (~1 mm in length), and binary PPAW FZs (~0.8 mm in length), and an increasing aspect ratio for ZrB_2 grains in PPAW welds (up to 40:1) compared to PAW ZrB_2 grain aspect ratios (up to 25:1) revealed that growth of ZrB_2 was hindered in PPAW FZs. Grain growth was also observed to decrease with decreasing arc power. A high arc power resulted in high growth rates of ZrB_2 and a textured FZ, whereas lower arc power FZs did not exhibit texture. A high current plasma arc (222 A) was used to increase the temperature of the weld pool, such that ZrB_2 growth would follow the arc thermal gradient. ZrB_2 growth occurred in the basal plane, resulting in grains with a plate-like morphology, where grain thickness increased by ledge growth. ZrB_2 grain sizes within the FZ were observed to affect the strength of weldments. PM flexure strengths were measured to be ~660 MPa and strengths were observed to drop to ~140 MPa for PAW weldments and ~170 MPa for PPAW weldments. Diffusion of C into the melt pool was observed to hinder ZrB_2 grain growth significantly (~150 μm maximum ZrB_2 grain size). The decreased maximum grain size resulted in average flexure strength of ~250 MPa for ZrB_2-ZrC-C weldments.

2.0 INTRODUCTION

Zirconium diboride (ZrB_2) is ceramic material belonging to the group of materials known as ultra-high temperature ceramics (UHTCs), where UHTCs are typically classified as ceramics with melting temperatures >3000°C.[1] Some of the properties that make ZrB_2 of interest include its high melting temperature (3245°C), high thermal conductivity (108 W/m·K), and chemical stability.[1-3] These properties make ZrB_2 attractive for applications such as molten metal crucibles, refractory linings, and hypersonic flight applications, such as atmospheric re-entry vehicles or rocket propulsion.[1,4-6] Due to the interest in using ZrB_2 for these applications, the ability to join ZrB_2 has also become of interest, where joining would be useful for both repair and complex shape fabrication.[7,8]

Brazing and solid-state techniques have received the most attention as potential joining techniques for UHTCs, but each have weaknesses.[7-9] For instance, palladium alloys have been studied for the joining of ZrB_2, but the melting temperature of these braze alloys are lower than the expected use temperature for several UHTC applications (>2000°C).[8,9] Solid-state joining, however, requires high temperatures and pressures to achieve dense joint microstructures. This can limit complex shape fabrication due to the processes typically utilized to densify UHTCs such as ZrB_2. Examining metal joining techniques reveals that fusion welding, joining by melting, is highly utilized for the joining of metals, but has received little attention for ceramic joining. Arc welding, fusion welding with an electric arc, is one of the most popular of these metals fusion welding techniques. With a low electrical resistivity (6 μΩ·cm), ZrB_2 may be an arc weldable ceramic, and fusion welding may be possible.[3,10,11]

Arc welding has previously been reported as a method of joining ZrB_2 based ceramics, but this research project presents processing-microstructure-property relationships that have not

been previously investigated.[10,11] A more fundamental study of the mechanical behavior of the joint aids in determining the usability of the joined material, while understanding the related microstructures is expected lead to process improvements. Knowledge of the arc welding process for joining ceramics can lead to the production of complex shape parts that may not have been previously possible.

3.0 EXPERIMENTAL PROCEDURES

3.1 Powder Processing

During the course of the project, several ceramics were processed and welded following the same basic procedures. These ceramics included: ZrB_2-ZrC, ZrB_2-ZrC-WC, ZrC-TiC, TiB_2-TiC, and TiB_2-TiC-B_4C. As the processing and welding methods were the same, and/or similar for each ceramic, the experimental procedure will focus on ZrB_2-ZrC ceramics. ZrB_2-ZrC ceramics with a nominal carbide content of 20 vol% were prepared. Starting powders were mechanically mixed by ball milling ZrB_2 (H.C. Starck; Grade B; Newton, MA) and ZrC (H.C. Starck; Grade B) with 1.25 wt% phenolic resin (Georgia Pacific Chemicals; Atlanta, GA) for a nominal carbon (C) content of 0.50 wt%, or ~1.5 vol%. Milling was carried out in acetone for 2 hours using tungsten carbide media. After milling, the powder slurry was dried using rotary evaporation to minimize segregation of the constituents. Dried powders were then ground and sieved to -60 mesh prior to hot pressing.

Billets nominally 46.5 mm by 30.0 mm by 5.0 mm of ZrB_2-20 vol% ZrC (ZrB_2-20ZrC) were densified by hot pressing. Hot pressing was performed in a graphite element furnace (Thermal Technology; Model HP20-3060-20; Santa Rosa, CA). The milled and dried powders were loaded into a boron nitride coated graphite die. The powder was heated at a rate of 50°C/min, under a mild vacuum of ~30 Pa (200 millitorr). A one hour isothermal reaction hold

at 1650°C under vacuum was performed to remove oxide contamination from the surface of the powders. After the reaction hold, the vacuum atmosphere was switched to flowing argon and a pressing pressure of 32 MPa was applied. A heating rate of 50°C/min was used to reach the final densification temperature of 1980°C. Pressing continued at temperature until recorded ram travel ceased for a period of 10 minutes. Pressed billets were removed from the graphite die and ground to a nominal thickness of 4 mm using a manual surface grinder (Chevalier Machinery Inc.; Model FSG-618; Santa Fe Springs, CA) and a 120 grit diamond grinding wheel (National Diamond Labs; Los Angeles, CA). Surface ground billets were cut using a diamond cutting wheel (National Diamond Labs) into smaller coupons for electrical resistivity measurements and welding. The densities of each coupon were determined using Archimedes method and the relative density was calculated based on the rule of mixtures theoretical density for ZrB_2-20ZrC (nominally 6.18 g/cm^3).

3.2 Welding

Cut billets were butt welded in a custom welding chamber consisting of a glovebox (MBraun; UNIlab ; Garching, Germany) modified with feedthroughs for a graphite element furnace (Figure 1) for pre-heating, cooling water for the furnace, a welding ground, power and gas for a plasma arc welding torch (Victor Technologies; Thermal Arc; PWM 300; St. Louis, MO), and electrical power. The glovebox was set to maintain an argon atmosphere between 100 and 450 Pa (1.0 and 4.5 mbar) over atmospheric pressure. A Thermal Arc® plasma arc welding system consisting of a coolant circulator (HE100A), power supply (ArcMaster 300S), welding console (WC-100B), weld sequencer (WC-1), and plasma arc welding torch was utilized for welding. The pre-heat furnace consisted of a graphite box with nominal inner dimensions of 12.7 cm by 12.7 cm by 5.1 cm, the graphite element, and removable top plate to serve as the

welding ground. The furnace was surrounded by ~22.0 mm of graphite felt and ~6.4 cm of refractory. Temperature was monitored using a type B thermocouple. To control welding speed, the welding torch was attached to a torch track (ESAB; Gothenburg, Sweden) that allowed for variable welding speeds. The entire inert welding chamber is pictured in Figure 2.

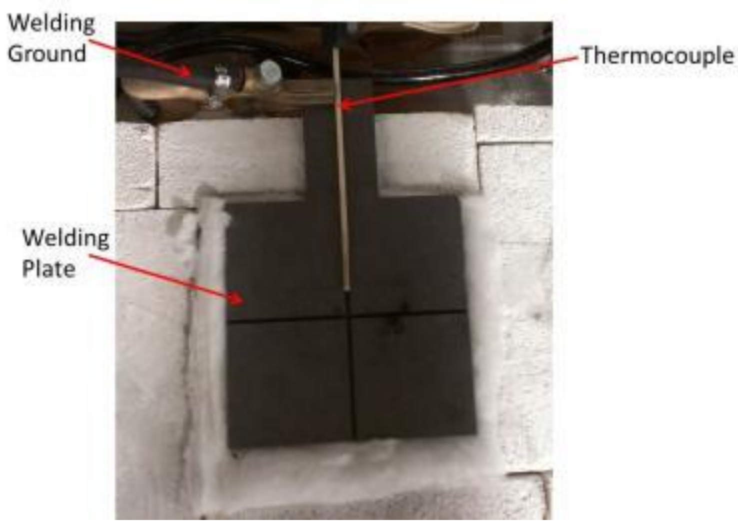

Figure 1: Covered welding furnace. The welding plate serves as contact with the specimen and ground. A graphite element under the welding plate heats the welding plate and the specimens to be welded. A type-B thermocouple measures temperature.

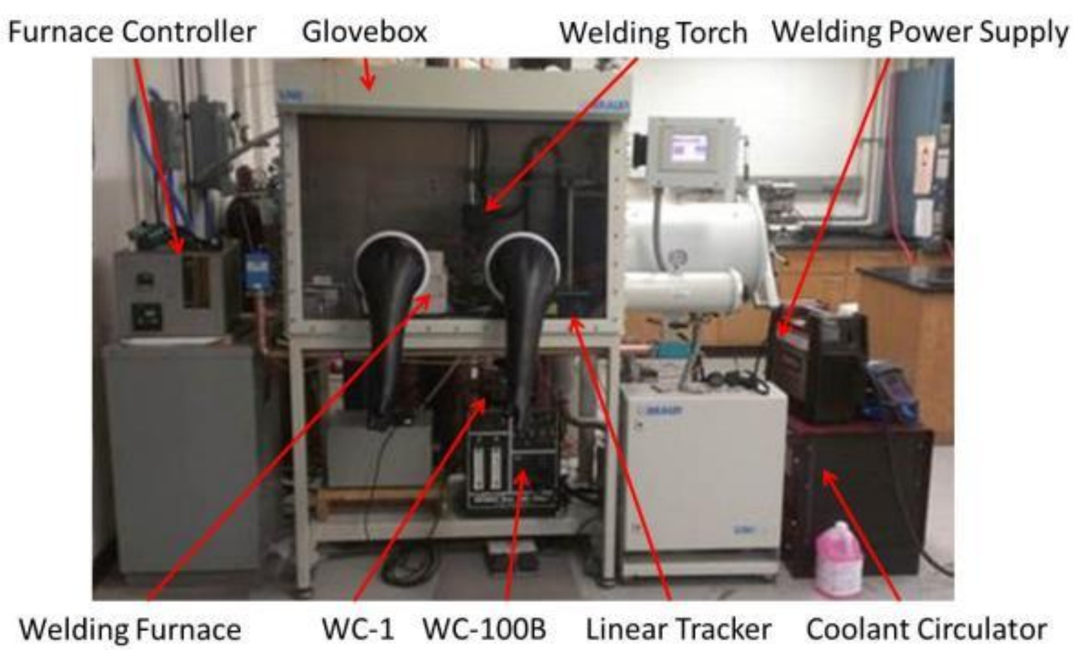

Figure 2: Welding chamber and equipment necessary for PAW of UHTCs.

Butt weld gaps were ~0.35 mm wide and formed by separating the diced samples with 4 layers of double sided tape (3M; Scotch® Double Sided Tape; St. Paul, MN). Samples were aligned with the torch, then covered with a layer of graphite felt and pre-heated to ~1450°C. Samples were uncovered and the torch track was moved such that the torch tip was placed at one end of the sample gap. The arc was struck to the sample, and the welding current was increased at a rate of ~20 A/s. Once the welding current was reached, the torch track was engaged at a speed of ~8 cm/min At the end of the weld, the current was tapered 10% over a time span of 0.25 s and decreased to a current of 25 A over 12 s. Welded samples were covered with graphite felt and the furnace was allowed to equilibrate its temperature. The furnace and welded samples were then cooled at a rate of ~30°C/min from the equilibrated temperature to room temperature.

3.3 Machining and Mechanical Testing

Mechanical properties of the ZrB_2-20ZrC parent material (PM) were analyzed. Parent material specimens were mounted in epoxy and polished to a mirror finish using successively finer diamond abrasives, with the finest abrasive being 0.25 μm. Vickers hardness was measured (Struers Inc.; Duramin 5; Cleveland OH) on polished surfaces using a load of 1 kg (9.8 N) for a dwell time of 10 s. Young's modulus (E) of the PM was measured by the impulse excitation technique (J.W. Lemmens Inc.; Grindosonic Mk5 Industrial; Heverlee, Belgium), as described by ASTM Standard C1259.[12] Fracture toughness (K_{IC}) of the PM was measured by the Chevron notch method, described by ASTM Standard C1421, using modified configuration A bars.[13] The modified bars were shorter (~23 mm) than the standard (45 mm), therefore the strain rate was adjusted to remain within the range specified in the standard. Flexure strength (σ) of the PM was measured by testing configuration B bars in four-point bending, described by ASTM Standard C1161, and analyzed with a Weibull distribution.[14] For comparison to the PM, ASTM C1161

configuration A bars were tested in four-point bending for three weldments, where the top surface of the weldment was placed in tension during testing. All flexure bars were cut from PM or welded billets using an automatic surface grinder (Chevalier Machinery Inc.; Model FSG-3A818) and a diamond cutting wheel. Cut bars were ground to size on an automatic surface grinder using a 600 grit diamond grinding wheel (National Diamond Labs). Fracture surfaces were analyzed using scanning electron microscopy.

3.4 Microscopy

Weldment specimens were cut perpendicular to the welding direction using a manual surface grinder and diamond cutting wheel. Cross-sections were mounted in an epoxy resin and polished to a mirror finish using successively finer diamond abrasives with the finest abrasive being 0.25 μm. Microstructural analysis of polished cross-sections was performed using optical microscopy (Nikon; Epiphot 200; Tokyo, Japan) and scanning electron microscopy (Hitachi; S-570; Tokyo, Japan). ZrB_2 grain sizes in the parent material and heat affected zones were determined by measuring the areas of at least 1000 grains from each weldment using ImageJ (National Institutes of Health, Bethesda, MD) and calculating the equivalent circular diameter. ZrB_2 grain sizes in the fusion zone were measured as the maximum Feret diameter.

4.0 RESULTS AND DISCUSSION

4.1 Fusion Welding of UHTCs

4.1.1 ZrB_2-ZrC Welding

Plasma arc welding was used to fusion weld ZrB_2-20ZrC. Figure 3 shows a stitched composite image of optical micrographs of the resulting fusion zone from two ZrB_2-ZrC coupons that were autogenously fusion welded by PAW, using a current of 198 A, a plasma flow rate of 0.75 l/min, and a welding speed of 8 cm/min. The weldment, referred to hereafter as "PAW",

exhibited full penetration through the fusion zone (FZ), and exhibited a keyhole at the end of the weld, a common feature associated with PAW.[15-19] The cross-section, taken 4.1 mm along the joint away from the beginning of the weld, shows a penetration depth of ~4.4 mm, and a measured cross sectional area of ~15.3 mm^2. The FZ of the PAW weldment also exhibited a convex surface and a concave heat-affected zone/parent material interface (HAZ/PM). With a low electrical resistivity, improved toughness due to second phase ZrC additions, and reduced melting temperature due to the ZrB_2-ZrC eutectic, PAW welding was shown to be a feasible joining method for ZrB_2-ZrC ceramics.

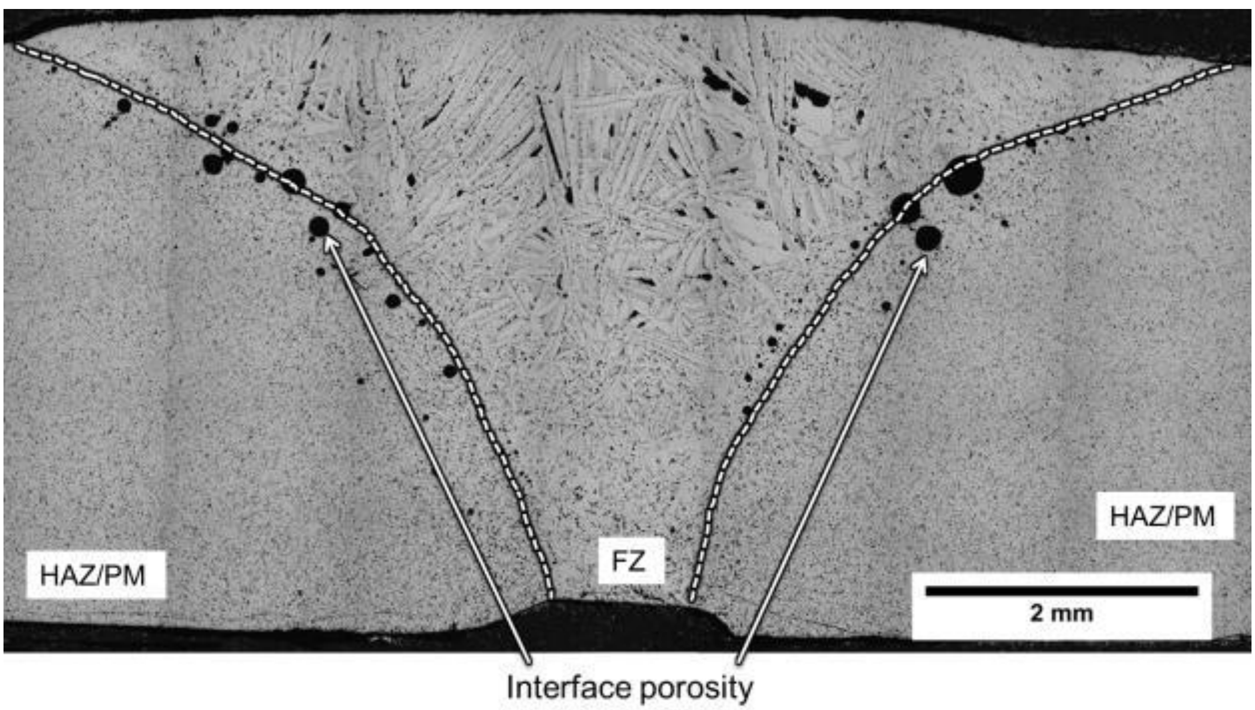

Figure 3: Cross-section of ZrB_2-20ZrC FZ taken ~4.1 mm from the start of the weld. Induced porosity (black) occurs at the interface of the FZ and the HAZ/PM.

A cross-section taken at 5.4 mm from the beginning of the PAW weldment revealed slightly less penetration, ~3.3 mm, showing that the penetration is not consistent throughout the fusion zone. The shape and microstructure of the FZ at 5.4 mm is similar to that shown in Figure 3 and was therefore not included in this report. Porosity within the FZ, and along the FZ

interface, was observed in both cross-sections. Image analysis of both cross-sections revealed the amount of induced porosity in the FZ was ~2.5 area percent (equivalent to 2.5 vol%, if the pores are randomly oriented). Along the interface, the largest pore diameter was ~310 μm. Within the FZ, the largest pore length was ~280 μm, with an aspect ratio of ~3.8:1. Pores along the FZ interface and within the FZ were likely to be formed by trapping plasma gas in the fusion zone after the closure of the keyhole. Porosity was observed along the interface, and throughout the FZ, where interface pores were circular and FZ pores were asymmetric.

Carbon is expected to be present in the weldment FZs due to excess C in the PM and residual C from the tape used to separate coupons before welding. Even though C was expected to be in the weldments based on the composition of the PM, analysis of the FZ for the PAW weldment revealed that no excess C was observed. Hence, the microstructure of the PAW FZ could be analyzed with the binary ZrB_2-ZrC phase diagram. Exaggerated growth of ZrB_2 (white phase) was observed in PAW weldments and an example is shown in Figure 4, where ZrB_2 grains grew to lengths up to ~1 mm. Without C in the FZ, ZrB_2 grains were allowed to grow uninhibited as the PAW weldment cooled through the ZrB_2 crystallization field in the ZrB_2-ZrC system. Measured aspect ratios ranged from 7.5:1 to 25:1 for ZrB_2 grains within the FZ, where smaller aspect ratio grains were observed at the top surface, and the bottom half, of the FZ. Growth of smaller aspect ratio grains occurred in greater quantities than larger aspect ratio grains. Nucleation and growth kinetics support these observations, as the surface of the FZ is expected to cool rapidly through convection. Similarly, the bottom side of the FZ is effectively in contact with a heat sink, the graphite spacer. Therefore, higher nucleation rates and lower times for the subsequent grain growth are expected near the top and bottom surfaces of the FZ, which should result in finer grain sizes. In contrast, the middle of the FZ remains hotter since

heat must transfer through the solidified outer layers, leading to increased time for grain growth.[20,21] As a consequence, ZrB_2 exhibited exaggerated grain growth within the FZ of the PAW weldment, where grains grew up to ~1 mm in length with aspect ratios as high as 25:1.

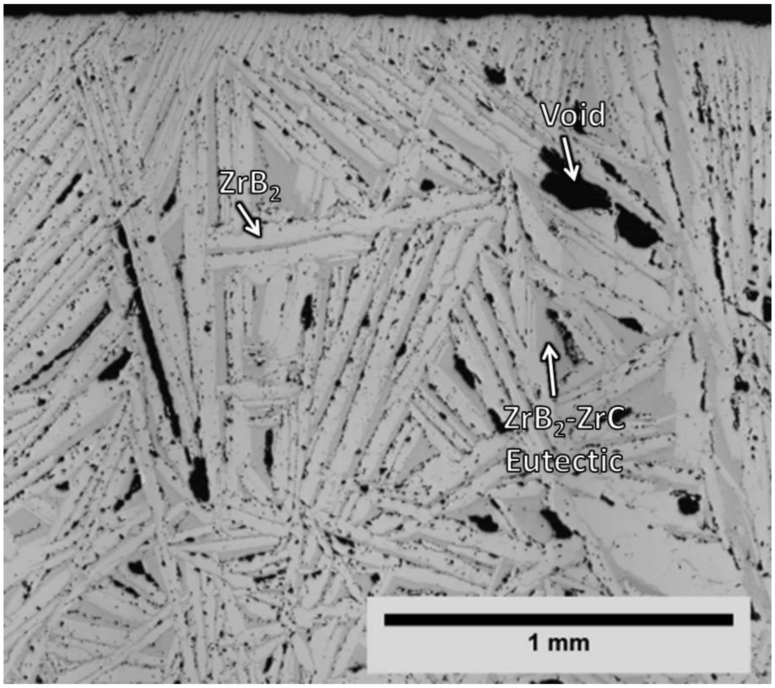

Figure 4: Optical image of the PAW weldment FZ exhibiting exaggerated growth of ZrB_2 (white) and void (black) formation in the FZ.

Within the FZ of the PAW weldment, the binary ZrB_2-ZrC eutectic phase exhibited a cellular eutectic structure containing ZrC rods surrounded by ZrB_2 (Figure 5). Image analysis of the cellular eutectic provided ZrB_2 and ZrC amounts in area percent, which was equated to volume percent due to the rod-like directional solidification. The ZrC content of the eutectic phase in the PAW weldment was 43.2±6.1 vol% (47.2±6.7 mole%). Hence, the observed eutectic composition was comparable, within the variance associated with image analysis, to the composition shown on the ZrC-ZrB_2 binary phase diagram, which is 39 vol% (43 mole% ZrC). Even though cooling occurred quickly, the composition and microstructure of the FZ of the PAW weldment is consistent with an equilibrium cooling path.[2]

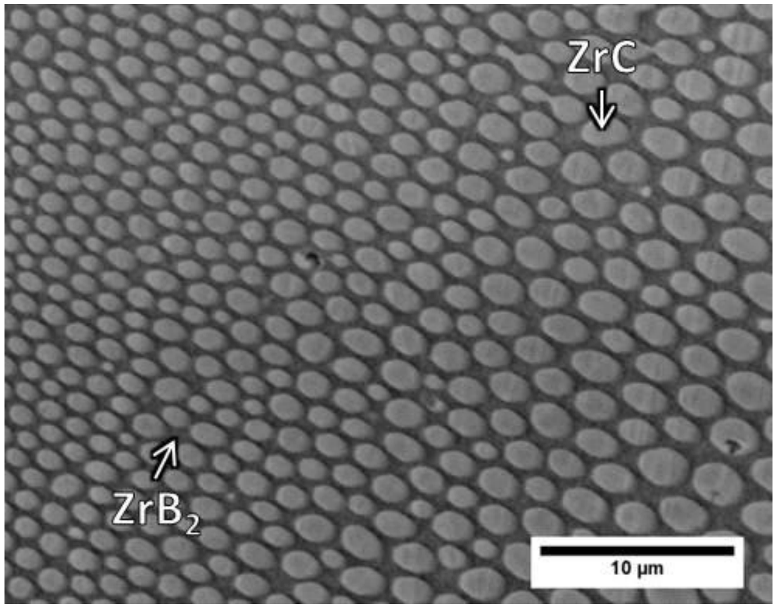

Figure 5: BEI of directionally solidified ZrB_2-ZrC eutectic in the PAW weldment. ZrC appears light grey and forms rods, solidifying in the direction perpendicular to the cross-section.

In an effort to limit the formation of porosity within the fusion zone, a notch ~1.1 mm wide and ~1.1 mm deep was added to the graphite disc that supports the specimens during joining. The notch in the graphite was aligned with the gap between the pieces being joined. Figure 6 shows how ZrB_2-20ZrC coupons were arranged for welding without and with a notch in the graphite disc. The notch under the joint should provide an escape route for any plasma gas that penetrates through the joint during keyhole formation, preventing the gas from becoming trapped in the melt.[18,19,22] Using the same parameters for the PAW weldment, ZrB_2-20ZrC was joined on a notched graphite disc to produce another weldment. The resulting FZ is shown as a stitched composite image of optical micrographs in Figure 7. Unlike the first weldment, the second weldment became attached to the graphite disc during PAW. The resulting weldment FZ cross-section was examined ~4.1 mm from the start of the weld. The weldment had a center depth of ~2.3 mm, and a cross sectional area of ~22.9 mm^2. The FZ had a concave surface, while the FZ retained a concave interface with the HAZ/PM, similar to the PAW weldment. Porosity along the interface was eliminated using the notched sacrificial graphite disc under the

ZrB_2-20ZrC coupons. Welding with a notched graphite spacer resulted in elimination of porosity, but reduced the penetration depth.

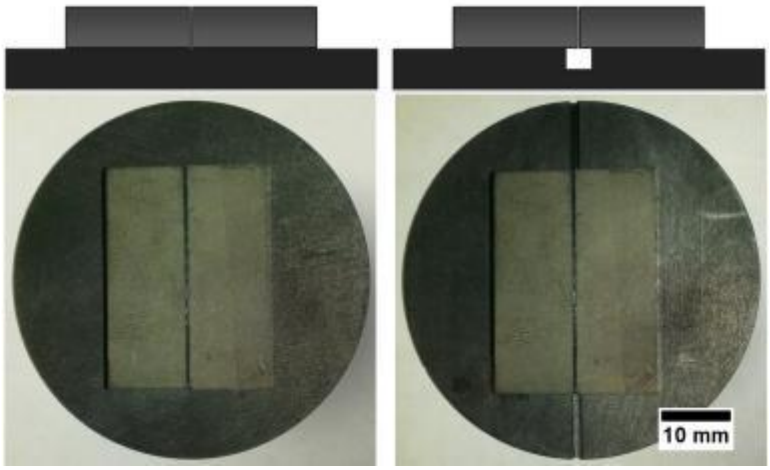

Figure 6: Schematic of graphite support disc (black) and ZrB_2-20ZrC (grey) coupons without (left) and with (right) a notch for escape of plasma gas during PAW.

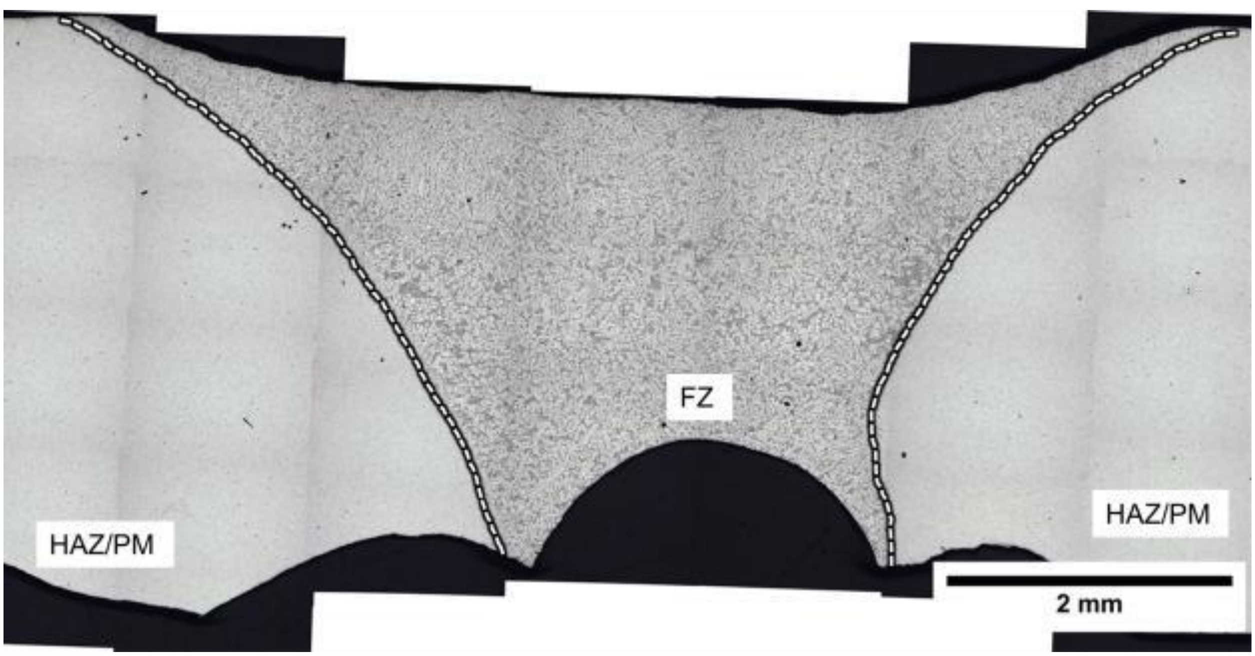

Figure 7: Cross-section of ZrB_2-20ZrC FZ taken ~4.1 mm from the start of the weld. Minimal porosity (black) was observed throughout the microstructure.

Microstructural analysis revealed significant differences between the PAW weldment and the second ZrB_2-20 ZrC weldment. Examination of the microstructure of the second weldment (Figure 8) at higher magnification showed that the eutectic in the FZ contained three phases. X-

ray diffraction of the FZ detected only two crystalline phases in the FZ, ZrB_2 and ZrC, despite the observation of three phases by electron microscopy. The FZ of the second weldment was attached to the sacrificial graphite spacer after PAW, so the black phase in Figure 8 is likely C, which would be difficult to detect by x-ray diffraction (XRD) due to its low x-ray scattering cross-section compared to ZrB_2 and ZrC. Raman spectroscopy was used to characterize the black phase from three different locations within the FZ, and revealed two peaks, one at 1333 cm^{-1} and one at 1585 cm^{-1}, corresponding to the diamond-like (D) and graphite-like (G) peaks for C.[23] Due to the presence of C in the FZ, the second ZrB_2-20ZrC weldment presented in this report will be referred to as "PAW C-rich". The eutectic composition shown on the ZrB_2-ZrC-C diagram presented by Rudy et al. is 80.6 vol% ZrB_2, 8.1 vol% ZrC, and 11.3 vol% C. However, the C content within the PAW C-rich FZ was 29.5 vol%, much greater than the C content shown on the phase diagram. Therefore, the cooling path of the FZ for the PAW C-rich weldment does not appear to be consistent with the Zr-B-C phase diagram.

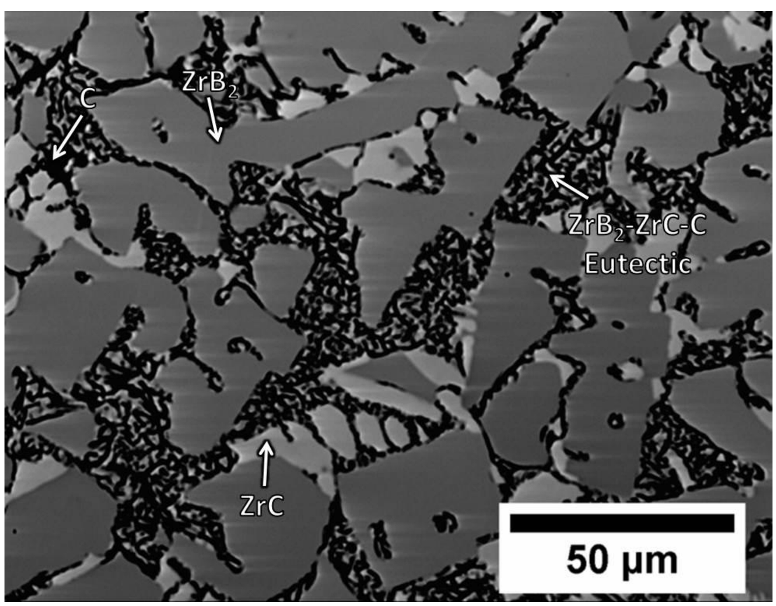

Figure 8: BEI image of the PAW C-rich FZ showing the presence of three phases, ZrB_2 (dark grey), ZrC (light grey), and C (black).

Comparing the FZs from the PAW weldment (Figure 4) and the PAW C-rich weldment (Figure 8), grain growth of ZrB_2 within the FZ was hindered when welding was performed using the notched graphite disc. While analysis of the PAW FZ revealed large, elongated grains of ZrB_2, more uniform growth of ZrB_2 and ZrC was observed in the PAW C-rich weldment. From Figure 8, both ZrB_2 and ZrC grew asymmetrically, so their grain sizes are based on the maximum Feret diameter of each grain. Within the FZ of the PAW C-rich weldment, ZrB_2 grains had an average maximum Feret diameter of 22.7±22.1 μm, with a maximum size of 148.6 μm. In the PAW C-rich FZ, ~17% of ZrB_2 grains were over 45 μm, leading to a large standard deviation. The average Feret diameter for ZrC was 10.8±8.1 μm with a maximum size of 59.2 μm. When compared to the length of ZrB_2 grains in the PAW FZ, both ZrB_2 and ZrC had smaller average grain sizes in the PAW C-rich FZ. ZrB_2 grain growth was hindered by the diffusion of C into the PAW C-rich FZ.

Pulsed plasma arc welding (PPAW) was utilized as an arc welding method to hinder the growth of ZrB_2 grains in the FZ, without the incorporation of C. PPAW of ZrB_2-20ZrC was accomplished using a pulsed arc with a peak current of 260 A and a 50% background current. Pulsing occurred at a time interval of 0.1s for peak current, and 0.2s for background current. The plasma flow rate was 1 l/min and the welding speed was 12 cm/min. Microstructural analysis of PPAW welds reveals that grain growth of ZrB_2 was affected by pulsing the weld current (Figure 9). Measurements of ZrB_2 grains in the PPAW FZ indicated lengths up to 0.76 mm, with aspect ratios ranging from 13.5:1 to 43:1. The larger grain lengths and lower aspect ratio grains in PAW welds reveals that PPAW hindered the growth, in both length and width, of ZrB_2 grains in the FZ. PPAW was used to weld ZrB_2-20ZrC and was observed to hinder the growth of ZrB_2 compared to PAW of ZrB_2-20ZrC.

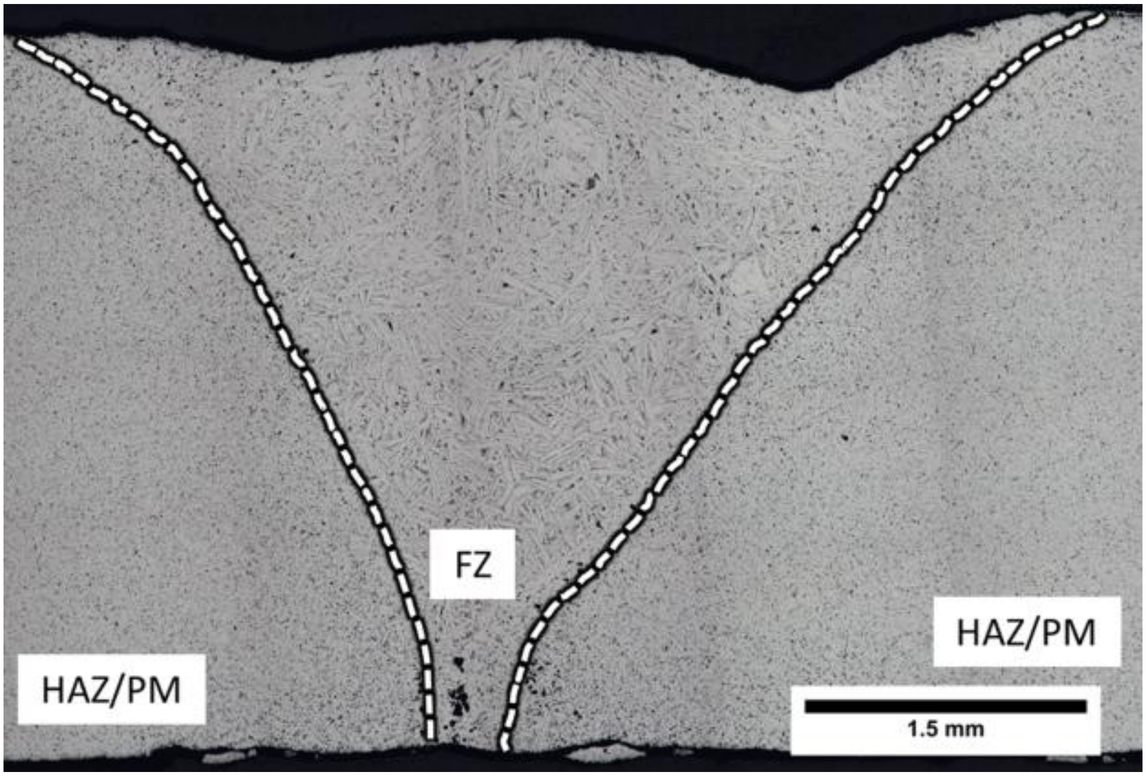

Figure 9: Optical micrograph cross-section of ZrB_2-20ZrC PPAW FZ exhibiting a reduction in ZrB_2 grain size and FZ porosity compared to ZrB_2-20ZrC PAW welds. The fusion zone (FZ) and heat affected zone/parent material (HAZ/PM) are identified.

4.1.2 TiB_2-TiC Welding

A successful butt weld of TiB_2-20TiC (welded using a current of 135 A, a plasma flow rate of 0.75 l/min, and a welding speed of 8 cm/min) exhibiting full penetration along the entire length of the joint is shown in Figure 10. Several welds were attempted with increased heat input, which was achieved by increasing current, or plasma flow rate. Higher heat input divided the weld pool and pushed it up the sides of the two coupons producing a cutting action, similar to plasma cutting. Likewise, specimens produced with decreased heat input through lower currents or plasma flow rates were not melted, meaning that a weld pool could not be established. A weld cross-section taken 3.2 mm from the start of the weld revealed that the weld pool contained large oval pores, ~1 mm at their largest diameter. The large pores were located at the edges and base of the weld pool and can be seen in Figure 10. The FZ appears semi-circular, and was measured

to be 10.4 mm wide at the top surface of the PM, and 3.9 mm deep at the center of the joint. A distinct HAZ was not apparent. During plasma arc welding, the plasma flow rate caused the weld pool to be partially blown up onto the top surface of the parent material. These ridges were not taken into account while measuring the fusion zone dimensions. Grazing incidence X-ray diffraction identified TiB_2 and TiC as the only crystalline phases present in the weld pool. A backscatter electron image (BEI), Figure 11, also revealed two phases. As with ZrB_2-20ZrC PAW, cellular eutectic was present in the TiB_2-20TiC weldment. Based on phase contrast, TiB_2 appears white in Figure 10 and dark grey in Figure 11, while TiC appears light grey in both figures. While large pores were formed during the welding process, a full penetration weld was formed via plasma arc welding using a current of 135 A, and a plasma flow rate of 0.75 l/min. Further, the weld contained the same two phases as the parent material, TiB_2 and TiC.

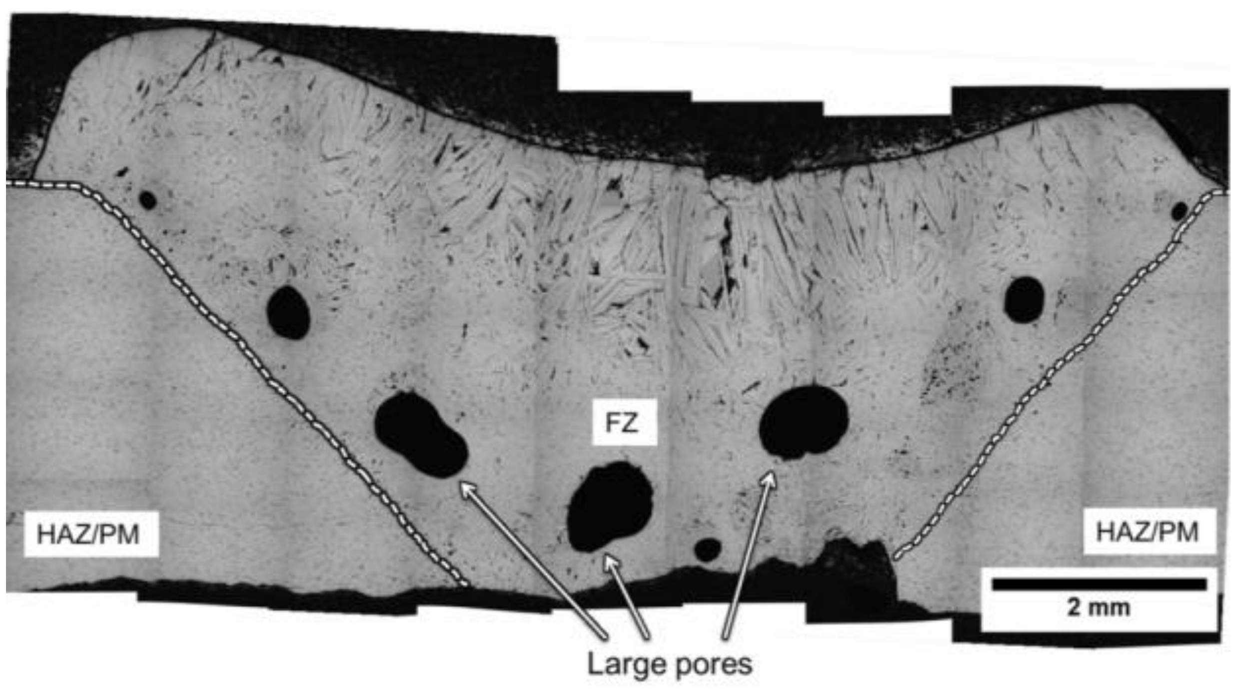

Figure 10: Cross section of a TiB_2-20TiC weldment showing directionally solidified TiB_2 grains (white) extending 1.9 mm into the FZ of a full penetration butt joint exhibiting full penetration. Arrows point to the large pores near the bottom of the FZ.

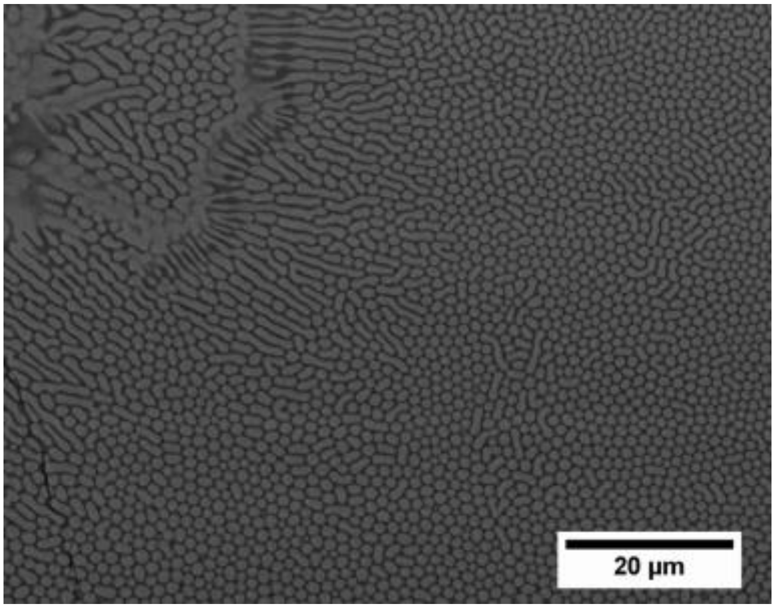

Figure 11: BEI of cellular eutectic that has solidified, perpendicular to the cross-sectioning direction/parallel to the welding direction.

4.1.3 ZrB_2-ZrC-WC Welding

PAW of ZrB_2-20ZrC and TiB_2-20TiC were demonstrated, but it was observed that the diboride exhibited exaggerated growth (grains up to 1 mm in length in one direction). Analysis of ZrB_2-ZrC PAW welding procedures also revealed that the growth of ZrB_2 could be controlled. Two methods were observed for control of grain growth. The first method was the incorporation of a third phase that may alter solidification. The second method was the use of PPAW, where controlled pulses provided the necessary heat to melt the PM at peak currents. To expand on both methods for control of ZrB_2 grain growth during weld pool solidification, PPAW was used to weld a ZrB_2 ceramic containing 25 vol% ZrC and 10 vol% WC (ZrB_2-25ZrC-10WC). Three FZs were analyzed. The first weldment was welded using a peak current of 260 A and a background current of 57% (148 A). Pulse times were 0.1s at peak and 0.3s at background. The plasma flow rate was 1 l/min, and the welding speed was 12 cm/min. The second ZrB_2-ZrC-WC weldment was welded using a peak current of 230 A and a background current of 57% (131 A). Pulse times, plasma flow rate, and welding speed were the same as the first weld. The third

ZrB_2-ZrC-WC weldment was welded using a peak current of 230 A and a background current of 50% (115 A). Pulse times were 0.1s at peak current and 0.4s at background current. Plasma flow rate and welding speed were the same as the first two welds. Representative microstructures for each weld are presented in Figure 12.

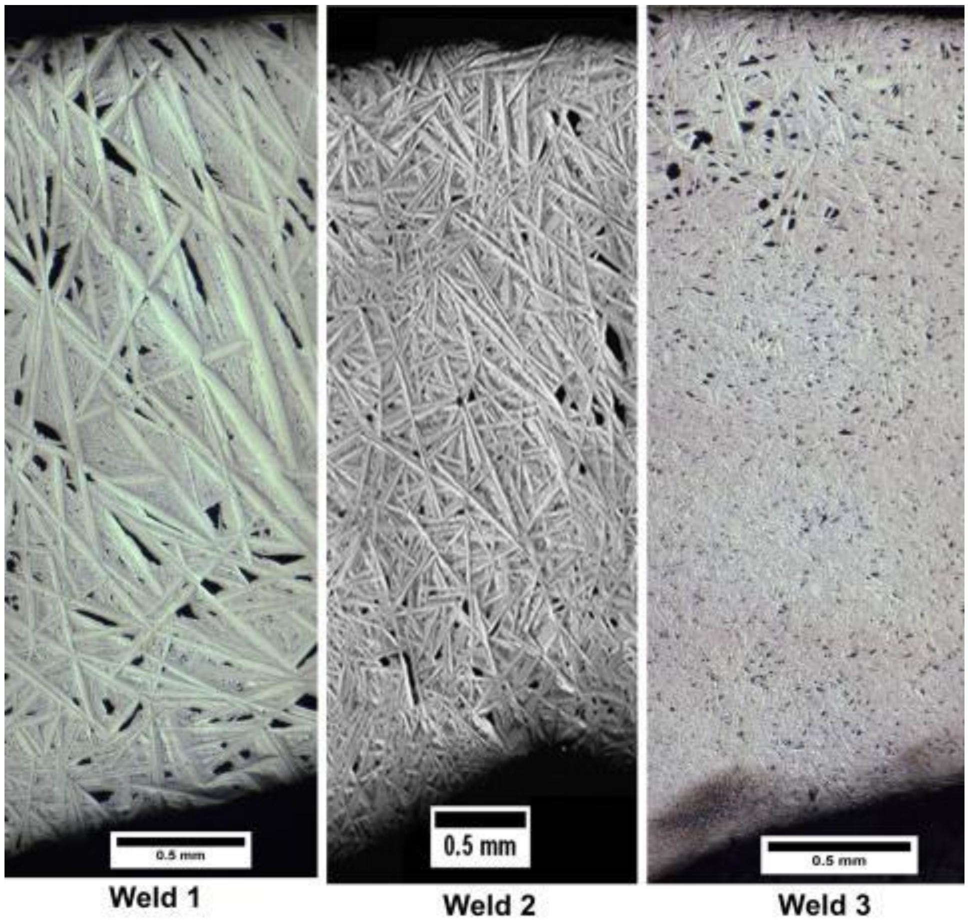

Figure 12: FZ microstructures of ZrB_2-25ZrC-10WC weldments.

The heat input for each of the three welds was calculated and heat input was observed to decrease from weld 1 to weld 3. Dividing the heat input by the welding speed gives the linear energy input in J/mm. The total linear energy input for weld 1 was 2637 J/mm, for weld 2 was 2333 J/mm, and for weld 3 was 2066 J/mm. The length of ZrB_2 grains was also observed to decrease with decreasing linear energy input, where ZrB_2 grains in weld 1 grew to lengths of 2.3 mm and ZrB_2 grains in weld 3 grew to lengths of 0.66 mm, a reduction of ~71% for the observed

maximum in ZrB_2 grain length. Therefore, decreasing the linear energy input hindered the growth of ZrB_2 grains in ZrB_2-25ZrC-10WC FZs.

4.1.4 ZrC-TiC Welding

PAW of ZrC containing 20 vol% TiC (ZrC-20TiC) was accomplished using an arc current of 198 A, plasma flow rate of 1 l/min, and a welding speed of 8 cm/min. A cross-section of the ZrC-20TiC weld (Figure 13) revealed that at the center of the weld, the FZ was 2.3 mm thick, but contacted the HAZ throughout the thickness of the coupon (4 mm). Porosity, oblong in shape and up to 0.9 mm in size, was observed at the edge of the FZ. Porosity and grain pullout were also observed in the HAZ. Areal analysis revealed that the C content increased from 0.4 area% in the PM to 1.7% in the HAZ, leading to increased grain pullout in the HAZ. X-ray diffraction detected the presence of TiO (hongquiite) in the PM, but not in the FZ, suggesting that pores in the FZ and HAZ are possibly formed from active oxidation of the carbide. Removal of oxygen impurities from the ceramic during processing may result in improved weldments. Based on these results, PAW appears to be a viable method for joining carbide ceramics.

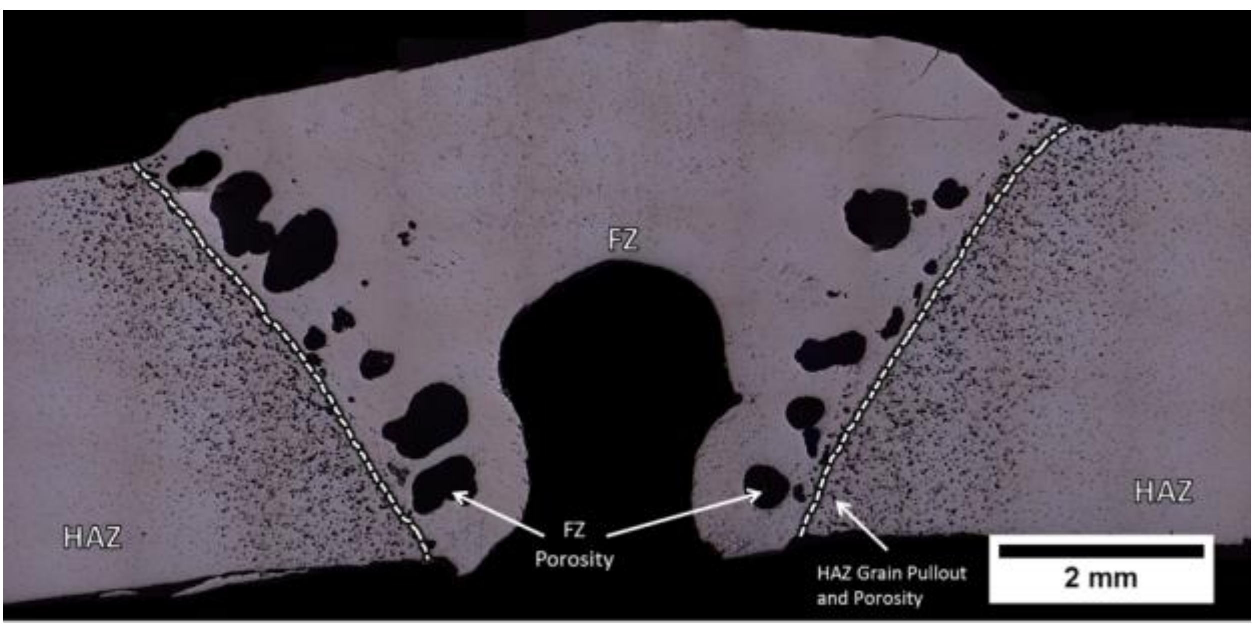

Figure 13: Optical micrograph cross-section of ZrC-20TiC joined using PAW. Porosity was observed at the edge of the FZ and HAZ, along with grain pullout in the HAZ.

4.1.5 W Filler Material

Tungsten filler (W wire) was added to the PAW FZ of ZrB_2-20ZrC. Filler was added to the FZ by feeding wire into the molten ZrB_2-ZrC weld pool just behind the plasma arc. W filler was added using a welding current of 200 A, 1 l/min plasma flow rate, and a welding speed of 8 cm/min. In the FZ (Figure 14), ZrB_2 grains were observed to grow up to lengths >1 mm with aspect ratios ranging from ~10:1 to ~45:1. The observed grain sizes were similar to that of ZrB_2 in PAW welds, with aspect ratios similar to both PAW and PPAW techniques. At a higher welding current and plasma flow rate, the incorporation of W as a filler may have affected ZrB_2 grain growth, but an in-depth analysis of filler materials and their effect on FZ solidification is required.

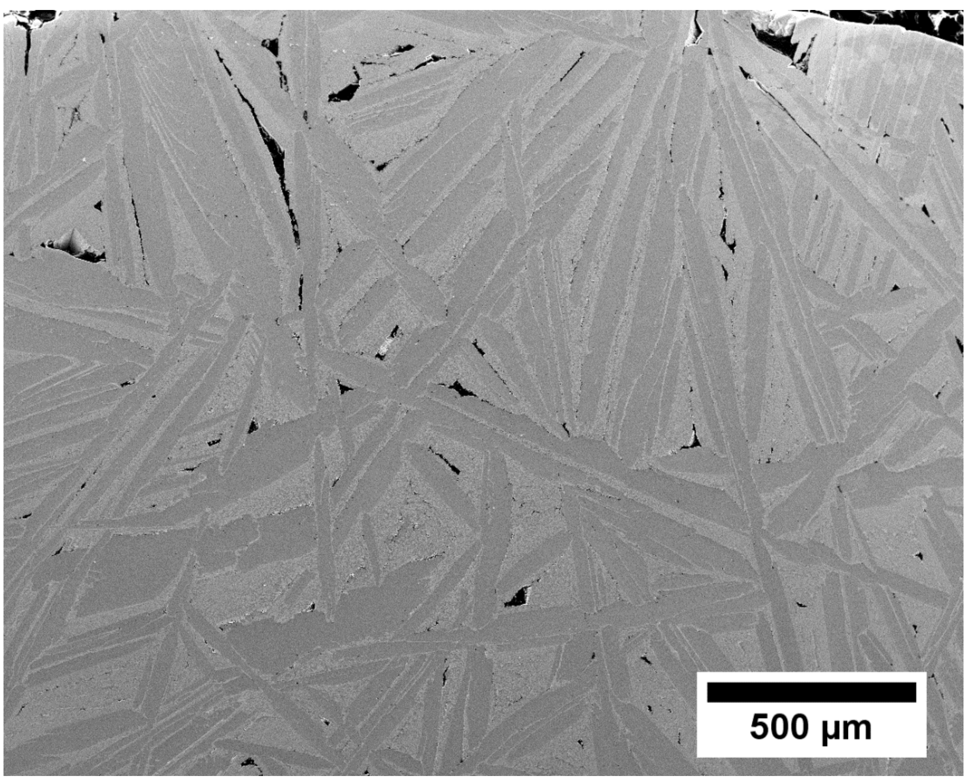

Figure 14: FZ of a ZrB_2-20ZrC FZ, where W was utilized as a filler material.

4.1.6 TiB_2-TiC-B_4C GTAW

Joining of a three phase PM was attempted by PAW of ZrB_2-ZrC-B_4C and TiB_2-TiC-B_4C ceramics. However, during welding loss of B_4C occurred, and the final FZ microstructure consisted of only ZrB_2-ZrC or TiB_2-TiC. Due to the penetration of the plasma jet into the weld pool, it is possible that oxidation of B_4C occurs during PAW of the three phase material. It should be noted that the argon gas utilized for a plasma gas contained oxygen impurities, therefore, oxidation of B_4C could occur even in the inert (typically <100 ppm O_2) environment of the glovebox. To determine if a diboride-carbide containing B_4C could be fusion welded, TiB_2-TiC-B_4C was welded with GTAW (gas tungsten arc welding) in metal container continuously flushed with argon. When compared to PAW, GTAW does not produce a plasma jet that penetrates the weld pool, therefore, the melt pool is not exposed to oxygen unless the welding environment contains oxygen. Welding was not performed in the glovebox, therefore, to reduce oxygen content, the metal container was flooded with argon for a period of 15 minutes prior to welding and continued during welding. Welding was performed by arcing to a graphite pillarthat supported the specimens. Radiative heating of the specimen from the arc was enough to pre-heat the specimens to a sufficient temperature to prevent thermal shock. Welding with a current of ~225 A, two specimens were butt welded using GTAW. After welding, the specimen was allowed to cool naturally to room temperature. The specimen was slightly glassy on the surface after welding, indicating that some oxidation had occurred.

SEM image analysis of the FZ revealed a finer microstructure, similar to that of PAW C-rich. Figure 15 presents a low magnification view of the FZ, where exaggerated growth similar to PAW of ZrB_2-20ZrC and TiB_2-20TiC, or PPAW of ZrB_2-20ZrC was not observed. Pores were observed at the HAZ/FZ interface, which may have formed due to oxidation of the weld

pool. Figure 16, a higher magnification image of the FZ, reveals the presence of two phases, a light grey phase, and a black phase. At the present time, it is unclear what the two phases are, or if a third phase is present, but not visible due to contract differences. However, TiC should appear as a brighter phase than TiB_2 in SEM, due to atomic number contrast. Similarly, a low molecular weight compound, such as B_4C would appear very dark compared to TiC or TiB_2. Regardless of the phases present, the GTAW FZ re-enforces the idea that GTAW can be utilized for the fusion joining of UHTCs.

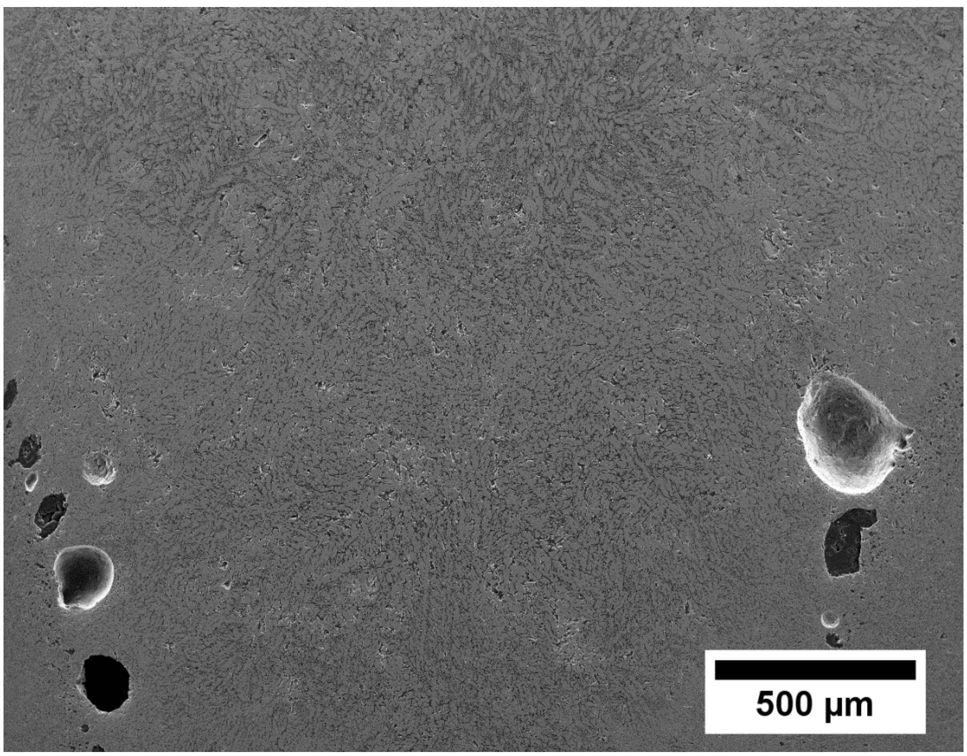

Figure 15: FZ of a TiB2-TiC-B4C weldment revealing a finer microstructure than PAW fusion joining methods. Porosity was observed at the HAZ/FZ interface.

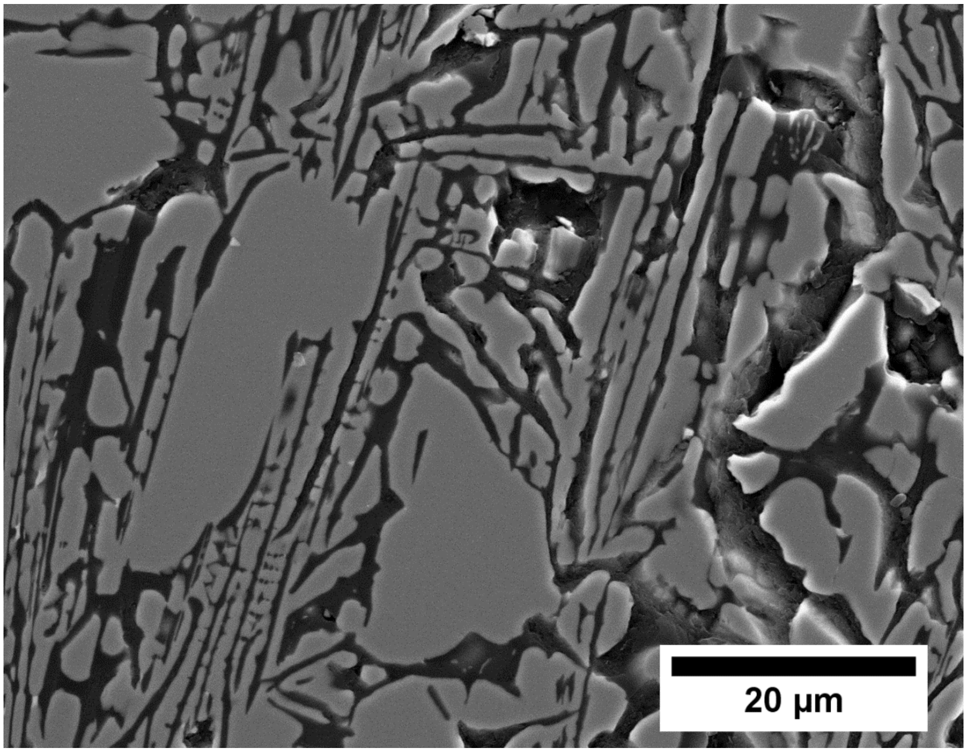

Figure 16: Higher magnification image where a phase with a high Z contrast and a phase with a low Z contrast were observed.

4.1.7 Applications for Welding UHTCs

This final sub-section on fusion welding presents demonstrations of fusion welding of UHTCs for fabricating components with complex shapes. The first example application demonstrated was a high temperature electrical contact. For the contact, a W wire (0.8 mm diameter) was spot welded to a ZrB_2 coupon (28.0 mm by 9.0 mm by 3.6 mm) using a welding current of 60 A and a plasma flow rate of 1 l/min. A representative image of a weld pool is presented in Figure 17. The W wire was curved into a “P” shape prior to joining to cover more of the side surface of the 9 mm by 3 mm ZrB_2 coupon, as shown in Figure 17. The weld pool area was 23.7 mm^2, which was ~73% of the coupon area. Partial melting of the W wire occurred. Excess W wire was observed at the far left, and the bottom, of the weld due to shifting

of the "P" during melting/welding. Porosity, Figure 17, was also observed at the surface of the weld. Below the FZ of the weld, cracking was observed in the ZrB_2 coupon. To reduce cracking, W wire was welded to ZrB_2-20ZrC coupons, which have a lower melting temperature (2830°C), lower elastic modulus (512 GPa), and higher strength (656 MPa) than monolithic ZrB_2 (T_m=3245°C, E=526 GPa, σ=570 MPa).[1,2,25] A lower melting temperature and elastic modulus reduce thermal residual stresses that may develop during cooling ($\sigma=\Delta\alpha\cdot\Delta T\cdot E$), while higher strength increases resistance to crack initiation.[26] Welds made on ZrB_2-20ZrC coupons covered >95% of the end of the coupon and exhibited porosity at the surface of the weld; however, cracking of the PM was not observed for ZrB_2-20ZrC coupons. Based on these preliminary studies, spot welding appears to be a viable technique for joining refractory metals to boride ceramics.

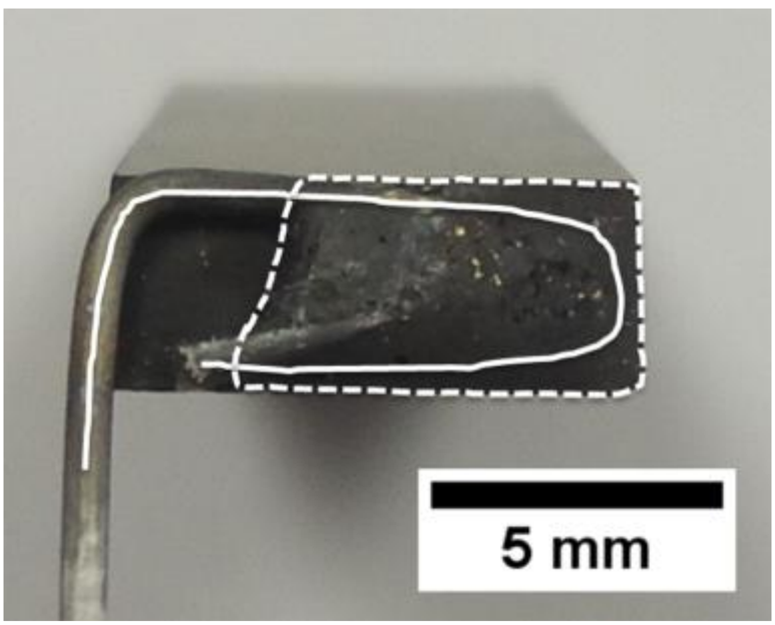

Figure 17: Spot weld of W wire onto a ZrB_2 coupon. A dashed line outlines the FZ and a solid line outlines the shape of the W wire prior to welding where a shift of the W wire at the bottom of the ZrB_2 coupon was observed.

Fusion welding was also used to fabricate an extreme environment UHTC thermocouple. Two thermocouple leads, one ZrB_2 and the other ZrB_2-20ZrC, were fabricated by extruding a

thermoplastic polymer (ethylene ethyl acrylate) loaded with the respective ceramic powders based on parameters discussed in previous studies.[27] For the present study, green filaments with a diameter of 2.4 mm were produced. After binder burnout to remove the polymer from the filaments, sintering was carried out at 2150°C for 2 hours. Sintered ZrB_2 filaments had a diameter of ~2.08 mm and ZrB_2-20ZrC filaments had a diameter of ~2.05 mm. Measurements by the Archimedes method revealed a relative density of ~60% for both the ZrB_2 and ZrB_2-20ZrC filaments. After sintering, the tips of a ZrB_2 and a ZrB_2-20ZrC filaments were joined by spot welding with a current of 60 A and a plasma flow rate of 1 l/min. The resulting thermocouple (Figure 18) was 54 mm in length, while the length of the fusion zone was ~3.5 mm. The voltage difference between the ZrB_2 and ZrB_2-20ZrC leads was measured as a function of temperature. Independent temperature measurements were made using a type B thermocouple. The thermocouple did not exhibit a voltage response below ~500°C; however, repeatable voltage differences were measured at higher temperatures. For example, the voltage difference was 0.12 mV at 750°C, 0.23 mV at 1000°C, and 0.46 mV at 1250°C. Voltage differences at higher temperatures were obscured by heating of the connections between the thermocouple and the multimeter due to the high thermal conductivity of the leads. Hence, PAW appears to be a viable technique for fabricating UHTC thermocouples.

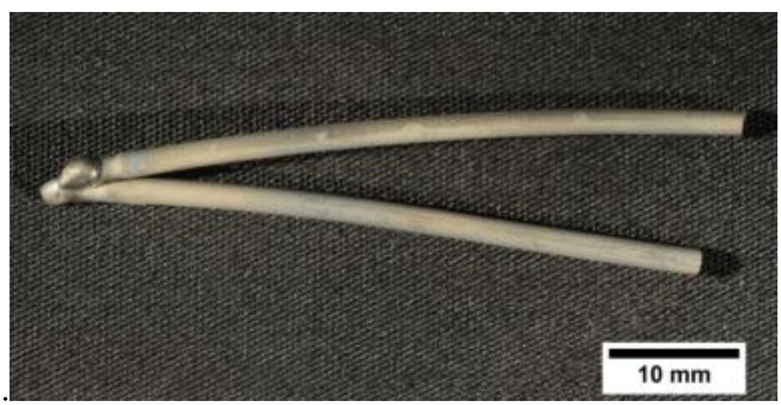

Figure 18: UHTC thermocouple fabricated from ZrB_2 and ZrB_2-20ZrC filaments.

The fabrication of a ZrB_2-20ZrC wedge, which was a mock-up of a wing leading edge for a hypersonic aerospace vehicle, was completed using PPAW. One face on each of two ZrB_2-20ZrC billets (nominally 45 mm by 30 mm by 4 mm) was ground at a 10° angle to produce a wedge with a 20° angle. The billets were then welded via PPAW using a peak welding current of 260 A with a 50% background current during pulsing. Pulse times were 0.1s at peak current and 0.2s at background current. The plasma flow rate utilized was 1 l/min, and the welding speed was 12 cm/min. During welding, melt back of the billets occurred and excess melt flowed to the side of the leading edge. Excess material was removed using wire electric discharge machining (EDM). The leading edge was cut in half to examine the FZ for porosity, and to measure the penetration depth of the weld and the amount of melt back from the tip. Porosity was apparent at the base of the weld pool; however, the FZ appeared to be dense, Figure 19. The penetration depth of the FZ was ~2.8 mm. The melt back of the billets after welding was ~4.5 mm. The hollow center of the wedge allows for the potential to cool the leading edge with a gas, liquid, or a higher conductivity solid.[28,29] The hollow center also decreases the mass of the leading edge compared to solid UHTC wedges. The welded presented in Figure 19 has ~16 area% void space, giving the hollow wedge a 16% reduction in mass compared to a solid wedge. PPAW was utilized to fabricate a hollow ZrB_2-20ZrC leading edge, demonstrating the ability to fabricate complex ceramic shapes by fusion welding.

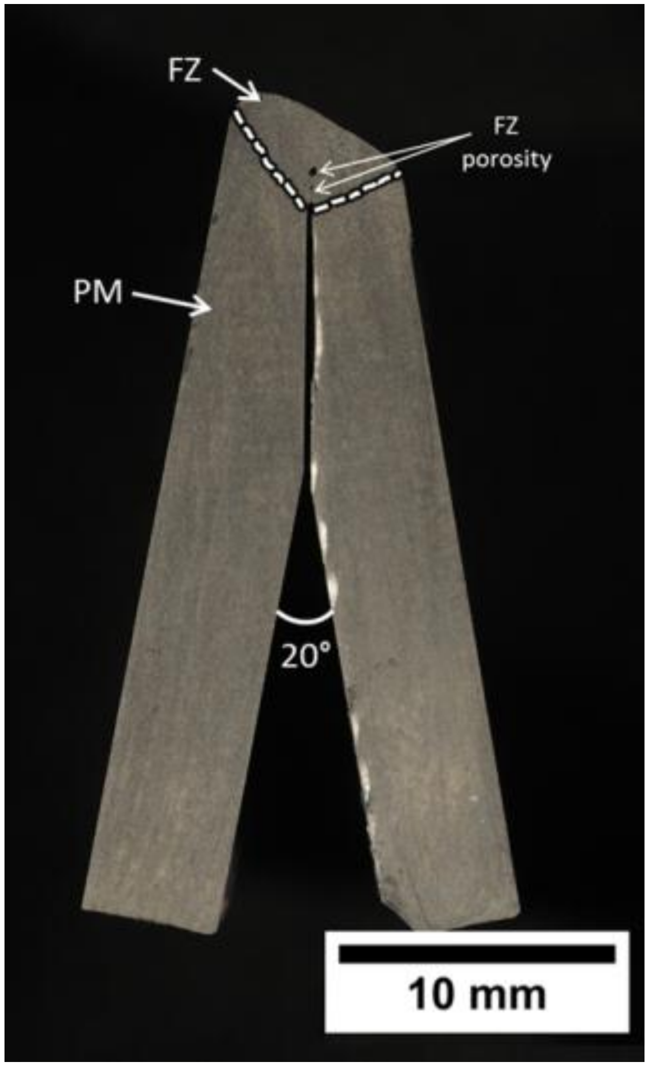

Figure 19: Hollow ZrB_2-20ZrC wedge. Porosity is observed near the base of the FZ.

4.2 Mechanical Properties

4.2.1 Parent Material Mechanical Properties

Mechanical properties measured for the PM are summarized in Table I. Vickers hardness was 15.2±0.1 GPa, which falls within the range of hardness values reported by Tsuchida and Yamamoto (14.5 GPa, 23 vol% ZrC) for ZrB_2-ZrC ceramic composites.[30] Young's modulus of the PM was 512±2 GPa.[12] A volumetric rule of mixtures of reported Young's moduli for single crystal ZrB_2 (526 GPa) and single crystal ZrC (406 GPa) suggests that the Young's modulus of the PM should be 502 GPa.[25,31] When compared to the rule of mixtures calculation, the

measured value is higher than expected. Assuming the value of 526 GPa is correct for the Young's modulus of ZrB_2 (the highest reported Young's modulus for ZrB_2), the Young's modulus of ZrC was estimated to be 456 GPa using a volumetric rule of mixtures and the measured Young's modulus of the composite. This value falls within the reported range for the Young's modulus of ZrC, which is 400 GPa to 470 GPa.[30,32] Therefore, the measured Young's modulus value is consistent with a fully dense ZrB_2-20ZrC ceramic. The values of both Vickers hardness and Young's modulus of the PM compare well with previously reported literature values.

Table I: Mechanical Properties of ZrB_2-20ZrC

Mechanical Property	**Value**
Hardness (GPa)	15.2±0.1
Young's modulus (GPa)	512±2
Flexure strength, average (MPa)	656±79
Weibull modulus	9.5
Fracture toughness (MPa·$m^{1/2}$)	7.0±0.4

The strength of the PM was 656±79 MPa, based on an average of 26 ASTM C1161 B-bars (4 mm by 3 mm by 45 mm) that were tested in four-point flexure. The strengths were further analyzed using a two parameter Weibull distribution.[14] Monolithic ZrB_2 has been reported to have four-point bend strengths up to ~570 MPa.[6] With an average strength of ~660 MPa, the PM ZrB_2-ZrC composite has a higher strength than monolithic ZrB_2, which has also been observed for similar particulate reinforced ceramic composites.[6,33,34] Similarly, the fracture toughness (K_{IC}) of the particulate composite is expected to be higher than the monolithic ceramic. The K_{IC} was measured to be 7.0±0.4 MPa·$m^{1/2}$ for the PM compared to values of 3.5-

4.5 MPa·m$^{1/2}$ reported for monolithic ZrB_2.[1] This value agrees well with a K_{IC} of 7.4 MPa·m$^{1/2}$ for a ZrB_2-ZrC composite containing 39 vol% ZrC from the technical literature.[35] The measured K_{IC} was higher than the reported K_{IC} of Tsuchida and Yamamoto, 5.1 MPa·m$^{1/2}$, for ZrB_2-ZrC containing 23 vol% ZrC.[30] The Weibull distribution was used to calculate a Weibull modulus of 9.5 for the PM. For commercial applications, a Weibull modulus of 10-12 is common, where a higher Weibull modulus indicates a narrower flaw size distribution, which allows for more predictable designs with ceramics.[36] The Weibull modulus of the PM is near that of commercial values for ceramics and the addition of ZrC led to an increase in strength and K_{IC} for the PM compared to monolithic ZrB_2.

4.2.2 Welded ZrB_2-20ZrC Flexure Strengths

Three weldments, PAW, PAW/C-rich, and PPAW, were tested in four-point flexure for comparison to the parent material. Flexure strength measurements were performed such that fracture occurred in the FZ of each weldment. Initially, fracture was observed in the HAZ of PAW/C-rich weldments, so an annealing procedure was utilized to reduce stresses. After annealing at 1500°C for 2 hours, fracture of PAW/C-rich flexure specimens occurred in the FZ. Fracture outside of the FZ did not occur in PAW or PPAW weldments, which were not annealed. The flexure strength of PAW weldments was 143±34 MPa, PPAW weldments were 166±22 MPa, and PAW/C-rich weldments were 247±21 MPa, which represent decreases in strength of 78% for PAW, 75% for PPAW, and 62% for PAW/C-rich compared to the PM. The lowest strength measured in the Weibull analysis of the PM was 509 MPa, and the highest strength for each weldment was 209 MPa for PAW, 205 MPa for PPAW, and 273 MPa for PAW/C-rich. This means that the highest PAW and PPAW weldment have strengths that are ~40% of the lowest PM strengths. In comparison, the strongest PAW/C-rich weldment had a strength that

was ~53% of the lowest strength measured for a bar of the PM. The average weldment strengths are comparable to those reported by Rice, where arc welded ZrB_2 based ceramics exhibited strengths ranging from ~100 MPa to ~210 MPa with a maximum strength of ~410 MPa for monolithic ZrB_2.[10] ZrB_2-20ZrC weldments had lower measured strengths compared to the PM, with weldments exhibiting strengths comparable to previously reported strengths for ZrB_2 based fusion welds.[10]

Measured mechanical properties, fractography, and Griffith criterion calculations were utilized to determine critical flaw sizes of the PM and each weldment. The failure origin of PM specimens were scratch-like flaws that had depths similar to the estimated flaw size of 29 μm, calculated using the Griffith criterion.[36] Thus, the strength limiting flaws were likely surface damage from machining of the specimens. K_{IC} of the weldments was not measured, but due to the large grain sizes in PAW and PPAW, and the C-rich nature of PAW/C-rich welds, a value of K_{IC} of 2.3 MPa·m$^{1/2}$ (comparable to the lowest K_{IC} values reported for monolithic ZrB_2) was used for calculating weldment critical flaw sizes.[37] Fractographic analysis of PAW weld pools revealed that a likely source for failure was circular penny cracks in the volume of the specimens (example shown in Figure 20). The formation of these types of flaws likely occur during cooling when the ZrB_2-ZrC eutectic solidifies and is pulled away from primary ZrB_2 that initially precipitates from the melt. Solidification of the eutectic results in volume contraction when going from a liquid to a solid. The observed flaw in Figure 20, a penny crack of ~280 μm in diameter, was smaller than the predicted size of 406 μm for the diameter of the penny shaped crack. While the measured flaw was smaller than predicted, similar flaws were observed in PAW weldment cross-sections (Figure 3), where penny shaped flaws up to 660 μm in diameter were observed. Hence, volume flaws may be considered a source of failure initiation.[24] Multiple

fracture mirrors were also observed on one ZrB_2 grain on a PPAW fracture surface (Figure 21). This indicates that spontaneous, or stress-induced, microcracking occurred in the ZrB_2 grains. Due to the anisotropic crystal structure of ZrB_2, residual stresses may result from differences in the coefficient of thermal expansion between the different crystallographic directions in the grains, which leads to cracking of grains.[25,38,39] Watts et al. previously estimated a band of grain sizes that may result in spontaneous microcracking of ZrB_2 as 980 to 2100 μm.[39] Lengths of ZrB_2 grains in FZs of PAW specimens fall into this range, suggesting that spontaneous microcracking of ZrB_2 grains could occur in the FZs of ZrB_2-ZrC joined by PAW. These microcracks may also link up, which would lead to the formation of volume flaws large enough to initiate failure. Therefore, initiation of failure in the FZs of ZrB_2-ZrC joined by PAW can occur from two different volume flaws (voids produced by liquid/crystal separation and linking of microcracks).

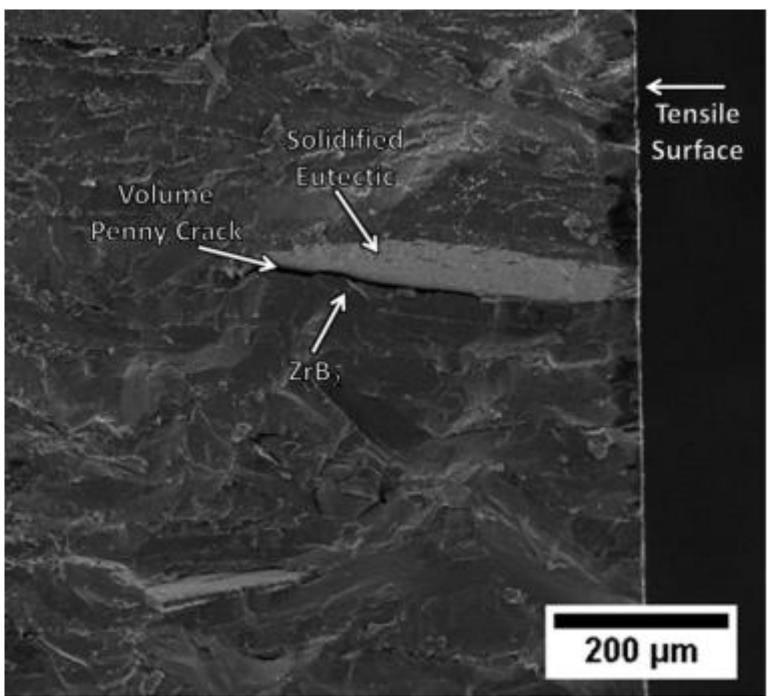

Figure 20: Backscattered electron image of PAW fracture surface where during cooling of the weld, eutectic pulled away from a ZrB_2 grain, leaving a penny shaped crack.

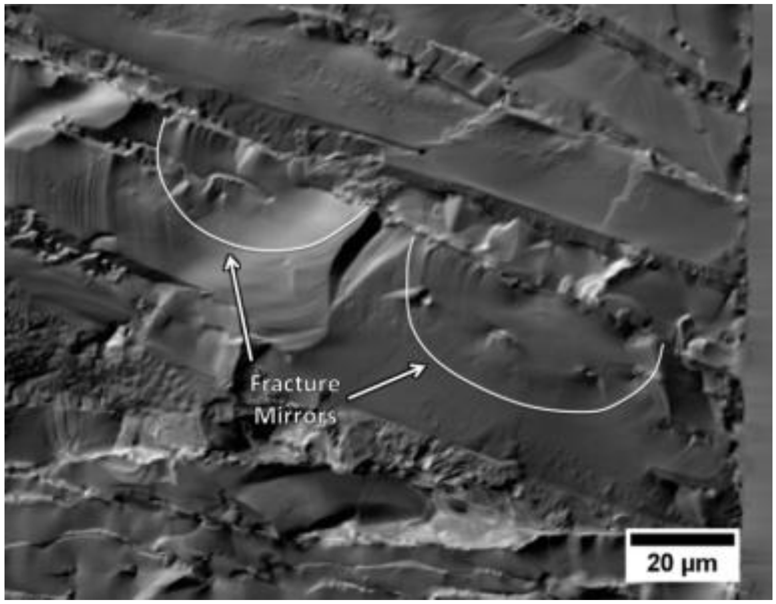

Figure 21: Multiple fracture mirrors were observed in one ZrB_2 grain in a PPAW weld.

In contrast, the lengths of ZrB_2 grains in PPAW welds were less than the range predicted for spontaneous microcracking. Hence, the fracture mirrors observed in Figure 21 were likely a result of stress-induced microcracking in the PPAW FZ, where link up of microcracks could result in a large enough volume flaw (calculated to be ~300 μm) to initiate failure. A volume critical flaw for PAW/C-rich was calculated to be ~140 μm (diameter) while a surface penny crack was calculated to be ~60 μm (radius), and a scratch-like flaw was calculated to be ~20 μm (depth). Machining with a 600 grit diamond wheel should leave scratches ~15 μm deep, while ZrB_2 grains within the PAW/C-rich FZ are also large enough to initiate failure, volume or surface, and specific critical flaws could not be defined for PAW/C-rich weldments. However, as with volume contraction in the solidifying eutectic in PAW FZs, tensile residual stresses may develop at the surface of PAW/C-rich weldments, which could also affect the weldment strength. The effects of these stresses appear to act on cracks radiating from a 30 kg (294 N) indent, placed near the surface of a PAW/C-rich FZ, as the cracks deflected towards the surface of the FZ (Figure 22). As the surface of the FZs were placed in tension during flexure testing, tensile

residual stresses may have led to weaker weldments by lowering the stress needed for crack initiation. Therefore, internal flaws (eutectic separation and microcracking), along with tensile residual stresses at the surface of weldments, lead to failure initiation of arc welded ZrB_2-ZrC weldments.

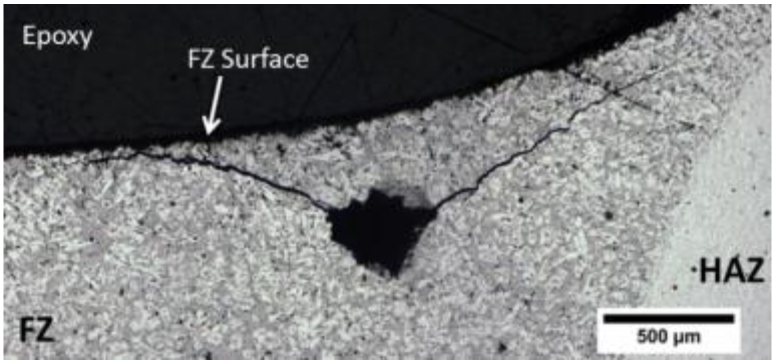

Figure 22: Cracking outlet from the corners of a 30 kg (294 N) Vickers indent in PAW/C-rich weldment. Cracks deflect toward the surface of the weldment.

4.3 Melt Solidification

Three sets of PAW parameters were used to fusion weld ZrB_2-20ZrC ceramics and estimate the heat input efficiency for PAW of ZrB_2-20ZrC. The three weldments were also compared to determine the effect welding parameters had on FZ solidification. Cross-sectional areas (from Figure 23) were 0.096 cm^2 for weldment 02 (176 A, 1.00 l/min), 0.132 cm^2 for weldment 11 (198 A, 0.75 l/min), and 0.086 cm^2 for weldment 20 (222 A, 0.50 l/min). Weld pool cross-sectional areas were normalized to a weld pool length of 1 mm, and the amount of material in the weld pool volume was used to estimate weld pool temperature. Weld pool temperatures ranging from ~22,000°C to ~67,000°C were estimated using estimated heat input efficiencies of 50-65%, but were deemed inaccurate. By assuming a lower melt pool temperature for each weldment, 5700°C, heat input efficiencies were estimated to be <24% for keyhole welds (weldments 02 and 11), and <18% for non-keyhole welds (weldment 20).

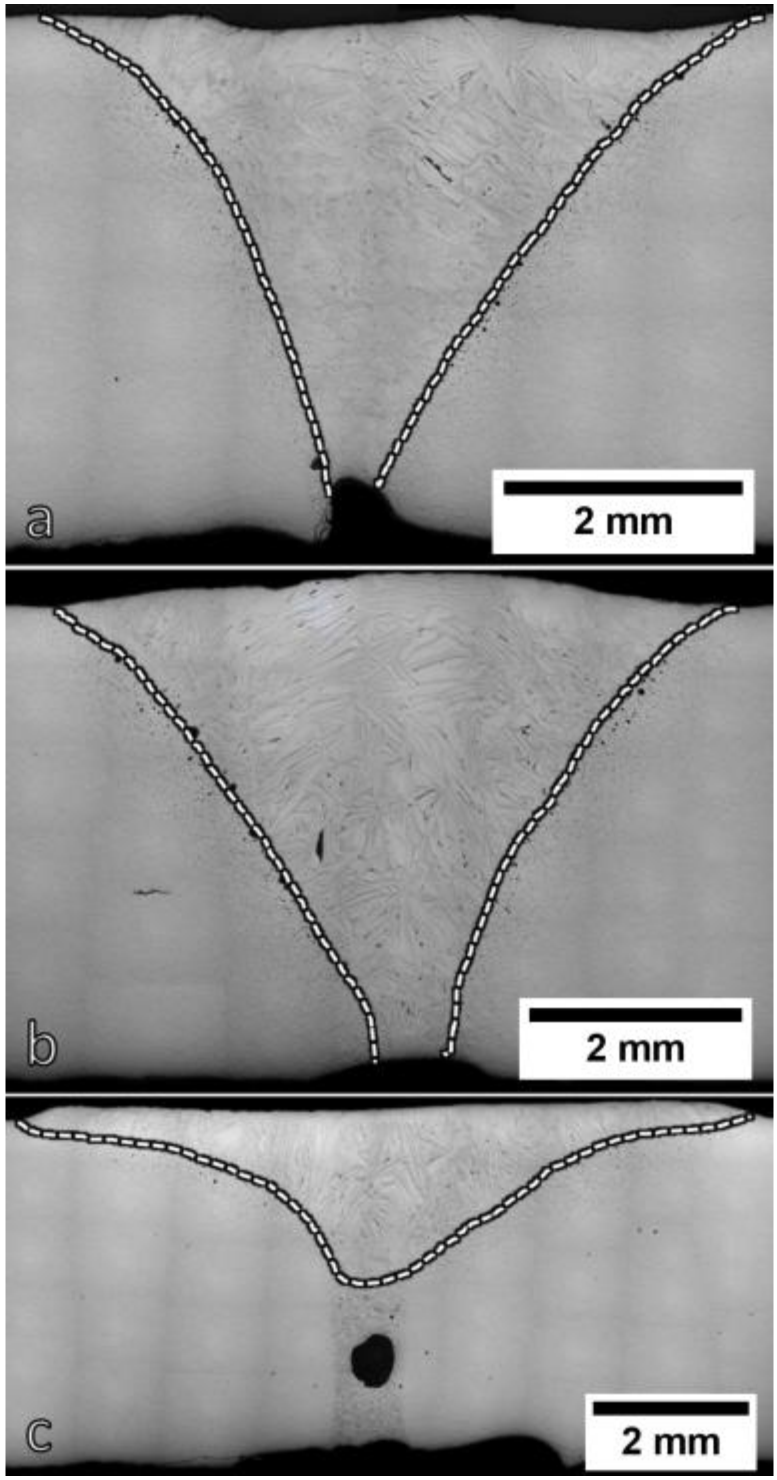

Figure 23: Three weldment cross-sections, cut perpendicular to the welding direction, with the FZ outlined. Weldment 02 (a) and weldment 11 (b) were considered full penetration keyhole welds, due to their cone-like appearance. Weldment 20 (c) was not considered to be a key hole weld.

EBSD was performed on the PM. A grain map and an inverse pole figure (Figure 24) were made from the crystallographic data to determine if texture was present in the PM. The distribution of ZrB_2 orientations in the inverse pole figure indicated that the PM had a random distribution of ZrB_2 crystallographic directions. White space in Figure 24 was the location of ZrC grains in the PM. The orientation of ZrC grains was mapped and the crystallographic orientation of ZrC was determined to be random, therefore orientation maps of ZrC are not presented herein. The crystallographic orientation of the PM was random, revealing that the PM did not have microstructural texture.

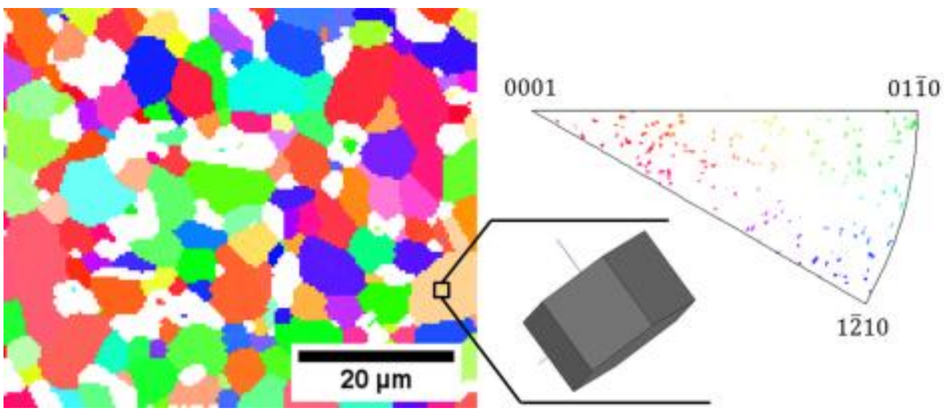

Figure 24: EBSD map of the PM with the corresponding inverse pole figure, where the PM exhibits random orientation. White space in the map on the left indicates the location of ZrC in the PM.

EBSD was also performed on 3 different locations within the FZ for each weldment. EBSD patterns were taken at the surface, middle, and bases of each FZ. White space within weldment FZ EBSD maps was the location of either ZrC or ZrB_2-ZrC eutectic, which will be discussed later, as current discussion will focus on mapped ZrB_2. In weldment 02, grains near the surface of the weld were the largest portion of the weldment, +100 μm grain lengths. This was observed in Figure 25a, where the ZrB_2 grains take up most of the EBSD map. Due to the large size of the ZrB_2 grains, the surface of the weldment 02 FZ appears heavily textured. Near the middle of the weld pool, the growth of grains was hindered (~65 to ~160 μm grain lengths),

and the number of grains was observed to increase (Figure 25b). The growth of ZrB_2 grains was observed to occur in clusters, or stacks, where grains growing within the same stack had the same crystallographic orientation. In the base of the weldment 02 FZ (Figure 25c), the frequency of ZrB_2 grains increased, while their lengths were similar to the middle of the FZ (~25 to ~170 μm grain lengths). Grain stacks were also observed at the base of the FZ, similar to those in the middle of the FZ. As the grain size throughout the FZ appeared to decrease deeper into the FZ, the FZ temperature is thought to have also decreased through the thickness of the FZ. Texture and grain size decreased, and the frequency of ZrB_2 grains increased, when moving from the surface to the base of the weldment 02 FZ. Globally (all inverse pole figures considered), the weldment 02 FZ had no texture.

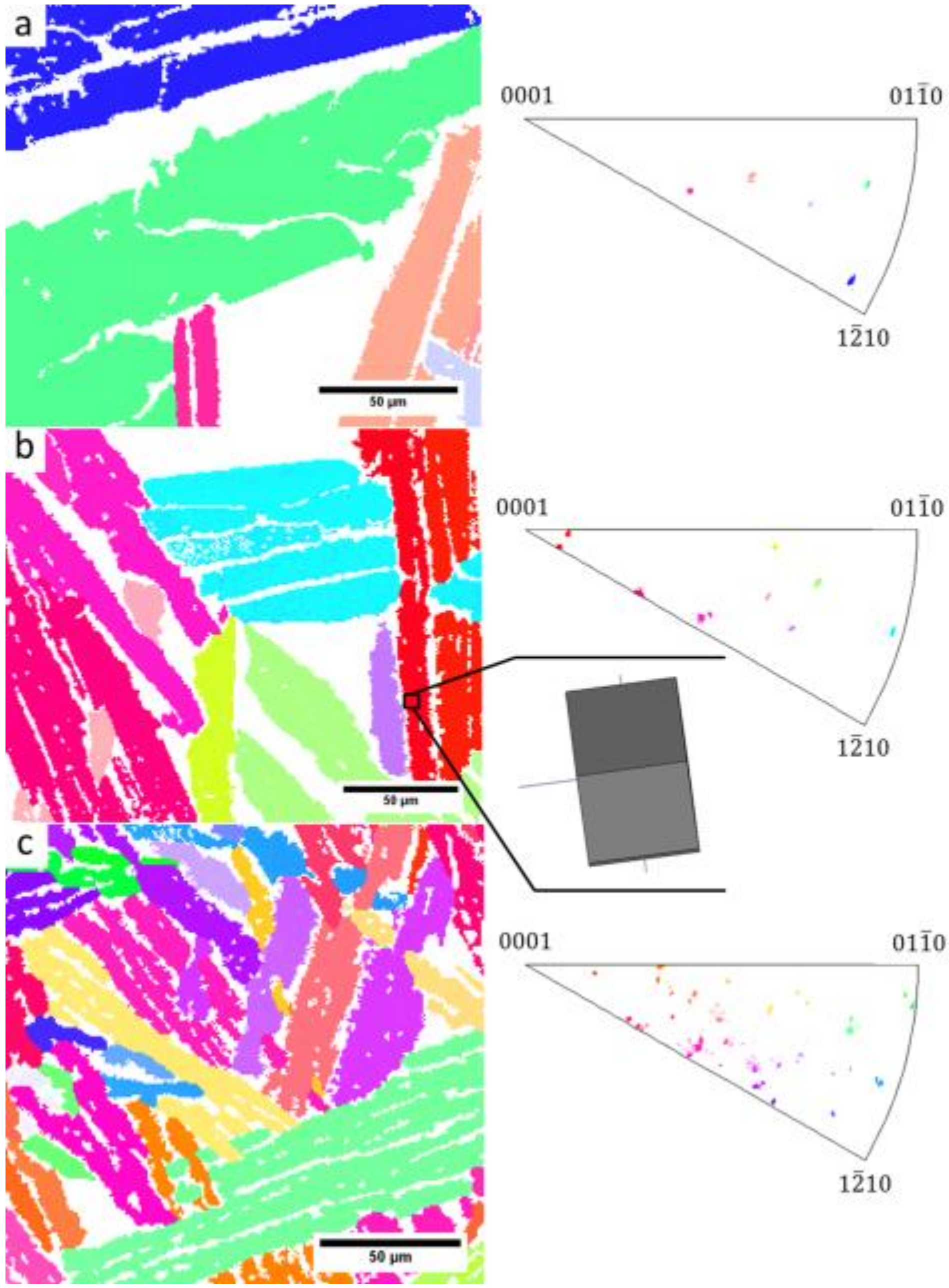

Figure 25: EBSD maps from near the surface (a), middle (b), and base (c) of the weldment 02 FZ and their corresponding inverse pole figures. A 3D hexagon represents the orientation of a specific grain.

EBSD maps of the weldment 11 FZ are presented in Figure 26. At the surface of the FZ grains ranged from ~40 to ~200 μm in length (Figure 26a). Weldment 11 did not have observed surface texture, like weldment 02, indicated by the increased number of points in the inverse pole figure (Figure 26a vs Figure 25a). However, similar to the middle of the weldment 02 FZ, grain

growth at the surface of the weldment 11 FZ occurred in stacks, and at a higher magnification, the surface of the weldment 11 FZ appeared to have more texture. In the middle of the FZ (Figure 26b), grain stacks were observed, but the number of grains within a stack decreased. ZrB_2 grains also increased in size (~80 to ~380 μm in length). The change in ZrB_2 grain size between the surface and the middle of the FZ is likely a result of temperature, as the middle of the FZ was insulated by the rest of the weldment, and the PM, during cooling. Or in other words, the middle of the FZ stayed hotter, leading to increased grain growth.[38] At the base of the weldment 11 FZ (Figure 26c), grain sizes were observed to be within a similar range to that of the surface, 25 to +140 μm in length. Grain stacks were also observed at the base of the weldment 11 FZ, but the number of grains within a stack was observed to be similar to the middle of the FZ. Texture was not observed to change throughout the weldment 11 FZ. Weldment 02 and weldment 11 had similar EBSD maps and inverse pole figures throughout the FZ, with the exception of the surface map for weldment 02. However, comparing Figure 23a and 23b, reveals that the microstructures of weldments 02 and 11 are similar near their surfaces, and the texture in Figure 25a was location dependent. Additional EBSD maps (not presented herein), based on other indexed locations at the surface of the weldment 11 FZ did appear to exhibit texture, like the surface of weldment 02. Grain lengths were similar at the surface and base of the weldment 11 FZ, but grain sizes increased in the middle of the FZ. Globally, the weldment 11 FZ was not textured. Weldments 02 and 11 were determined to have similar microstructures and microstructural textures, therefore, the temperature profiles of the two FZs were likely similar.

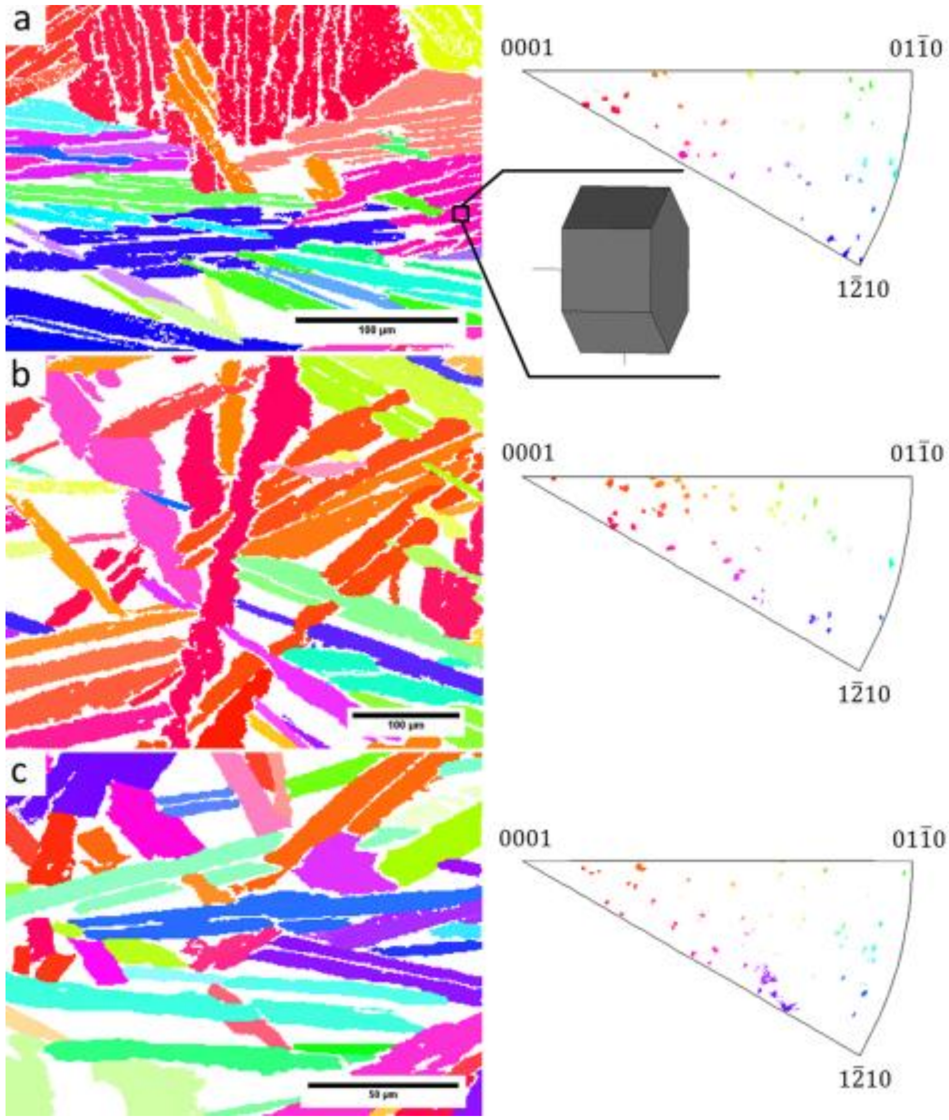

Figure 26: EBSD maps from near the surface (a), middle (b), and base (c) of the weldment 11 FZ and their corresponding inverse pole figures. A 3D hexagon represents the orientation of a specific grain.

Grains in the weldment 20 FZ were larger than grains in the FZs for weldments 02 and 11. ZrB_2 grains in Figure 27 were observed to be larger than the image, therefore, ZrB_2 grains in the weldment 20 FZ were estimated to be between ~100 and +200 μm in length. Similar grain sizes were observed throughout the depth of the weldment 20 FZ. Large ZrB_2 grains give the appearance of texture at the surface (Figure 27a) and base (Figure 27b) of the FZ. As the depth of the weldment 20 FZ was only ~2.3 mm, the FZ base was similar in depth to the middle of the

weldment 02 and 11 FZs. A third location at the side of the FZ was indexed (Figure 27c), and the side of the FZ also exhibited texture. At each location, grain stacks were observed. As weldment 20 was expected to have the highest weld pool temperature, the growth of grains was likely the dominant solidification mechanism, compared to the nucleation of new grains.[38] Hence, weldment 20 contained the largest observed ZrB_2 grains and the weldment 20 FZ had texture at the micro and global levels.

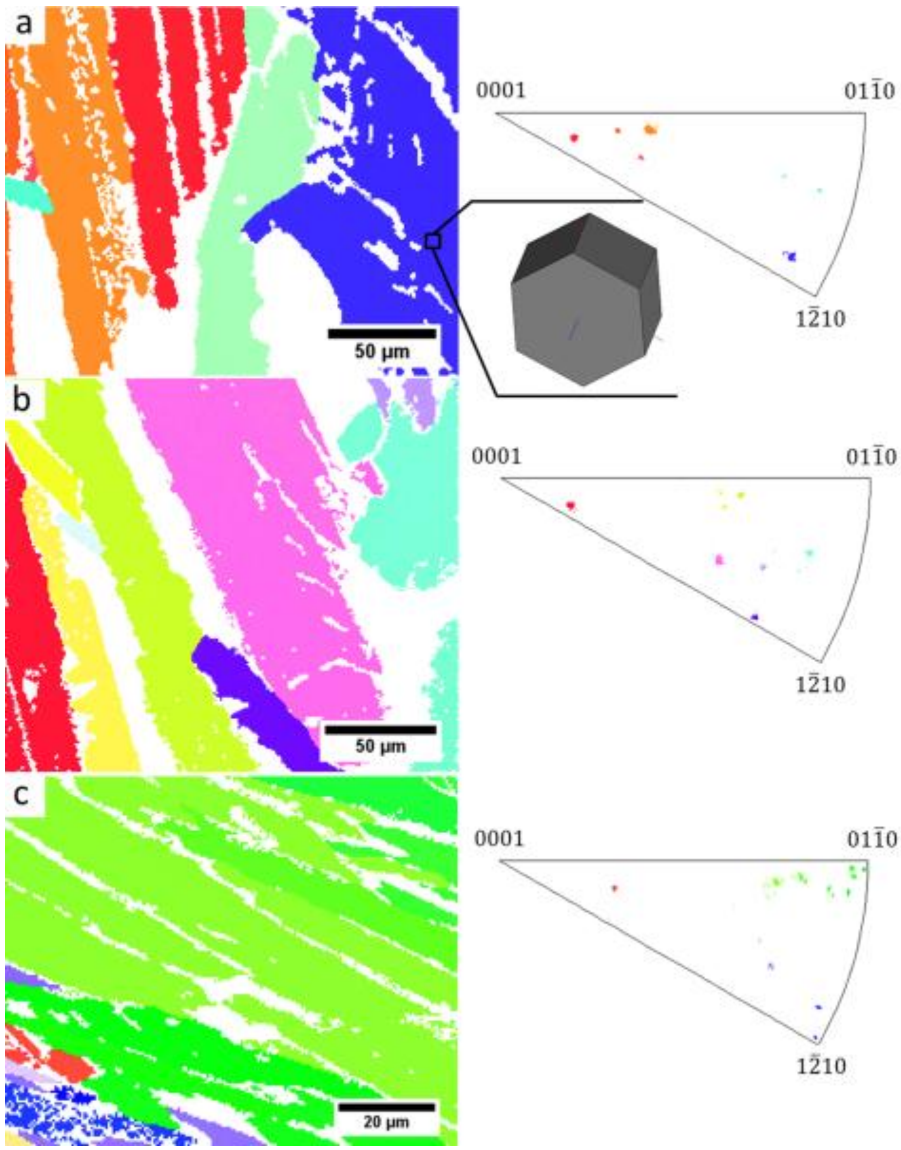

Figure 27: EBSD maps from near the surface (a), base (b), and side (c) of the weldment 20 FZ and their corresponding inverse pole figures. A 3D hexagon represents the orientation of a specific grain.

4.3.1 ZrB_2 Growth

Due to the exaggerated growth (preferred growth in one direction) of ZrB_2 in the weldment 20 FZ, the surface of the weldment was examined from a top-down perspective, or the area of arc impingement. A stitched optical image of the FZ surface (Figure 28) reveals that the weld pool diameter was not consistent, and varied from 5.9 mm (bottom of Figure 28) to 6.8 mm (top of Figure 28) in width. At the center of the FZ, ZrB_2 grains were observed to grow in the welding direction, with ZrB_2 grains growing to lengths of >2 mm. The direction of growth agrees well with the notion that for arc welding processes, the arc creates the largest thermal gradient, and grains will grow in that direction.[39] As the grains at the surface follow the known arc thermal gradient, EBSD indexing of the weldment 20 surface (Figure 29) was used to determine how ZrB_2 grains grew after nucleation. The surface appeared highly textured and indicated that ZrB_2 grain growth was in the basal plane, giving ZrB_2 a plate-like structure. Further analysis on a fracture surface of a previously welded specimen (same welding parameters as weldment 11), revealed a free surface, and ledge growth of ZrB_2 was observed (Figure 30).[39,40] Thus, ZrB_2 grains were determined to grow along their basal plane, increasing their thickness by ledge growth mechanisms.

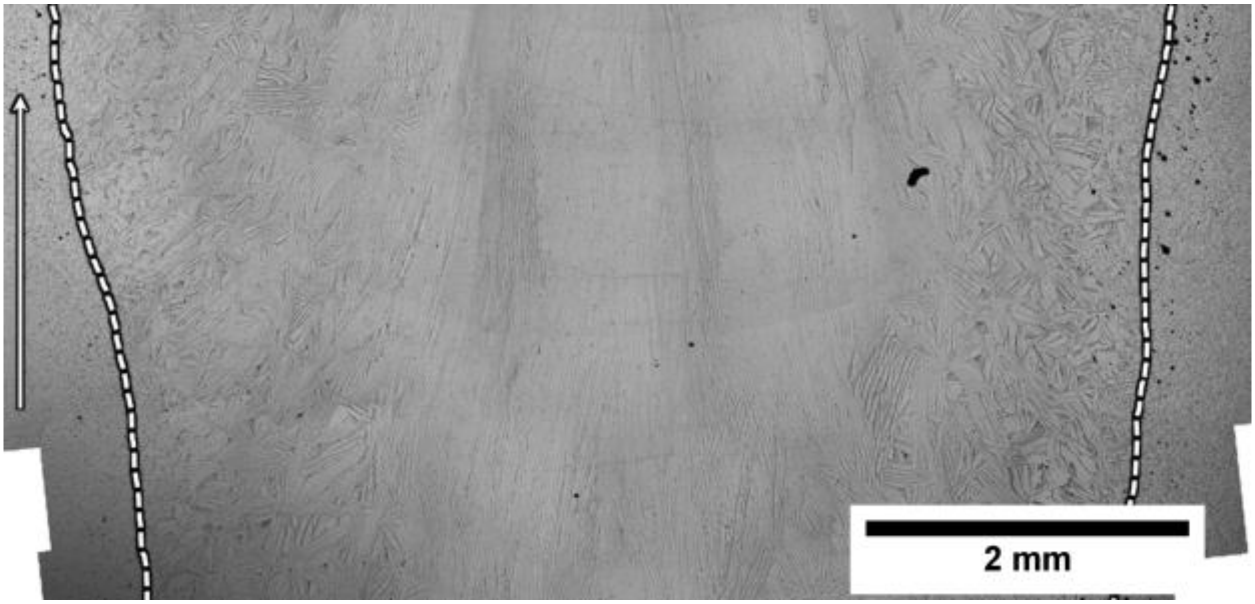

Figure 28: A top-down (surface of arc impingement) optical image of the weldment 20 FZ. The FZ is outlined, and an arrow points in the welding direction. Grains were observed to be as long as 2 mm in length, growing in the direction of the arcs thermal gradient.

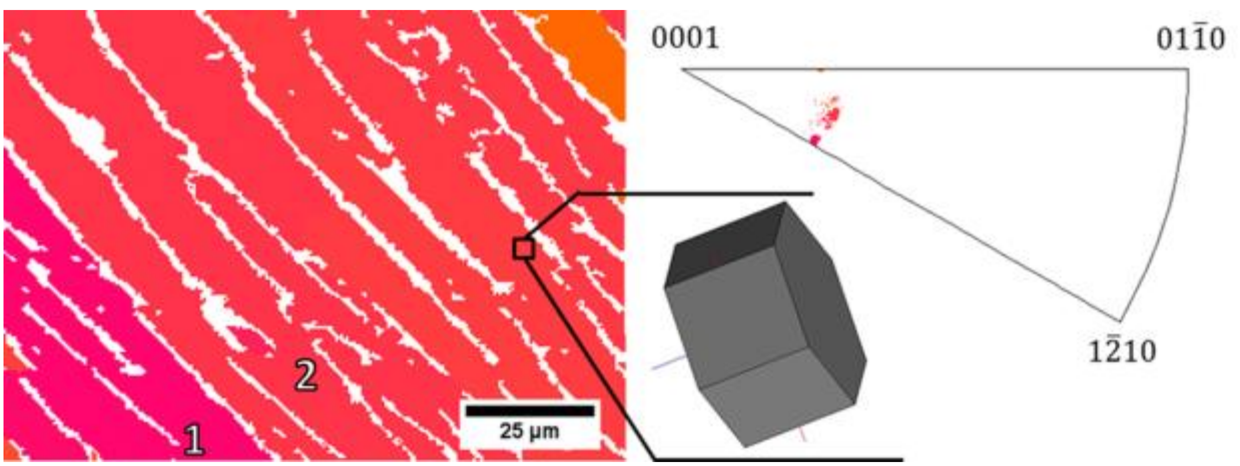

Figure 29: EBSD map from the top-down surface of the weldment 20 FZ and the corresponding inverse pole figures. A highly textured surface, grain growth occurs in the direction of the arcs thermal gradient. A 3D hexagon represents the orientation of a specific grain.

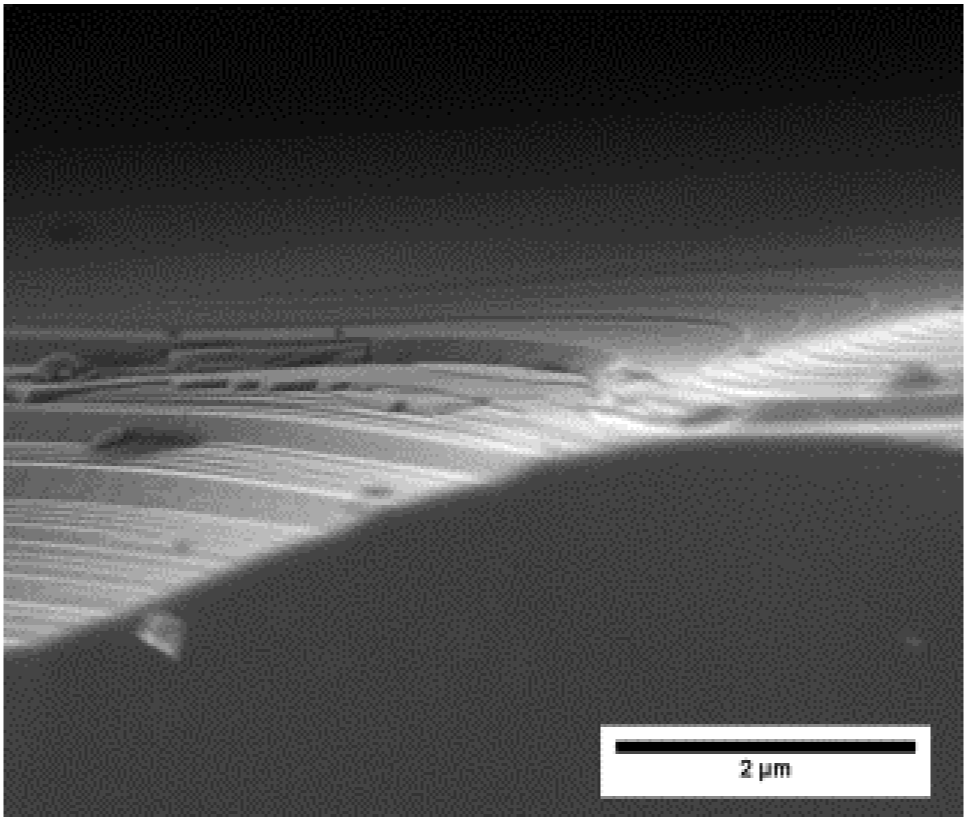

Figure 30: Secondary electron image of a weldment 11 fracture surface, exposing a free surface, where ledge growth of ZrB_2 was observed.

4.3.2 ZrC Precipitation

The formation of cellular ZrB_2-ZrC eutectic was observed in each weldment, but it should also be noted that the presence of the eutectic was not observed between ZrB_2 grains in a grain stack. Rather, between the ZrB_2 within a stack, only ZrC is present. It was determined that these regions do not solidify on an equilibrium cooling path, but, when ZrB_2 nucleates and/or grows at high enough rates, the weld pool liquid becomes desaturated of B, forcing the precipitation of ZrC from the liquid. As previously mentioned, this occurs within ZrB_2 grain stacks, and it can be observed that a ZrB_2 grain will "split" as ZrC begins to precipitate. Demonstrated with the secondary electron image of the Figure 29 EBSD map, Figure 31 shows two ZrB_2 grains of different orientations that had split and grew around ZrC. This suggests that

instead of a grain stack, consisting of individual ZrB_2 grains of similar orientation, a ZrB_2 stack at the surface of weldment 20 is one grain. Splitting of the grain stack was also observed in the higher nucleation regions of weldment 02 (middle and base) and weldment 11 (surface, middle, and base), where stacks of the same orientation were connected. EBSD indexing of ZrC within a ZrB_2 stack/grain revealed multiple orientations of ZrC, indicating that ZrC did not precipitate based off of the crystallographic orientation of ZrB_2. Precipitation of ZrC occurred through the formation of the equilibrium ZrB_2-ZrC eutectic (equilibrium solidification), or by forced precipitation as rapid growth of ZrB_2 desaturated the weld pool liquid of B (non-equilibrium solidification), also revealing that a stack of ZrB_2 grains was not multiple grains, but a single grain.

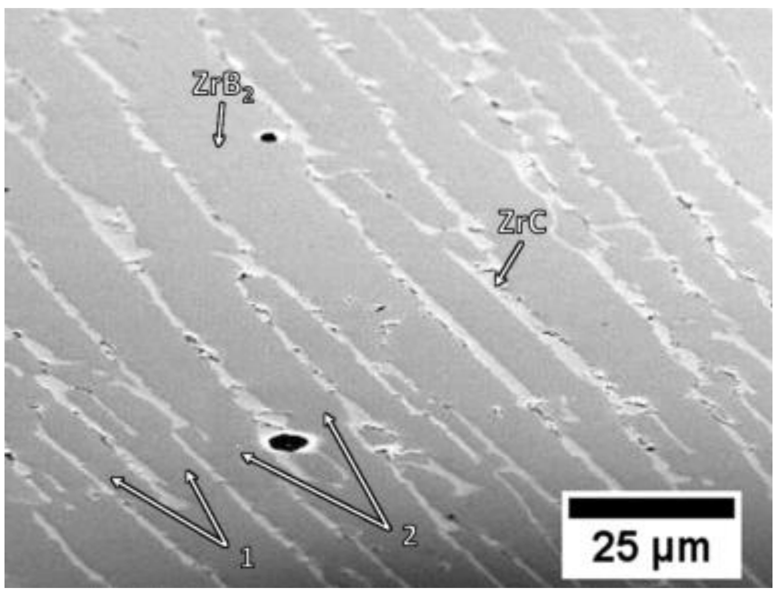

Figure 31: Secondary electron image of the weldment 20 FZ surface. Splitting of ZrB_2 within the same grain stack. Points 1 and 2 correspond to points 1 and 2 in Figure 29. Image tilted 72° relative to electron beam for EBSD indexing.

4.4 Plasma Jet Testing

Six welded ceramic components and one parent material were submitted to Dr. Michael Cinibulk at AFRL/RXCC, WPAFB, OH for plasma jet testing (CLIN 0003). Below is a detailed description of each sample:

1 Parent material (PM) wedge

1 Plasma arc welded (PAW) wedge

1 Pulsed plasma arc welded (PPAW) wedge

2 Plasma arc welded (PAW) plates

2 Pulsed plasma arc welded (PPAW) plates

The parent material composition was ZrB_2 containing 20 vol% particulate ZrC (ZrB_2-20ZrC). All welded specimens were cut parent material that was welded back together. Before welding, all specimens were pre-heated at a heating rate of 50°C/min to a temperature of 1450°C. After welding, the specimens were held at temperature for ~5 min, and cooled at a rate of 20°C/min to room temperature. Each welded plate is marked on the back side with an arrow to indicate the welding direction. Due to an error during welding, one of the PPAW plates was welded at a slower speed, as such, the PPAW plates are marked 1 and 2. The welding parameters are listed in Table II. PPAW current and pulse times are presented in the format "peak/background". After welding, the specimens were ground flat on top and bottom using a 600 grit diamond machining wheel, wedges were ground to an angle of 12°. Finish grinding of the specimens was performed by hand on a 600 grit polishing pad. Specimen images are included as Figures 32 to 34.

Table II: Welding parameters of ZrB_2-20ZrC specimens

Specimen	Welding Current (A)	Pulse Time (s)	Plasma Flow Rate (l/min)	Welding Speed (cm/min)
PAW wedge	180	N/A	0.75	8
PPAW wedge	270/140	0.1/0.2	1	12
PAW plates	180	N/A	0.75	8
PPAW plate 1	270/140	0.1/0.2	1	12
PPAW plate 2	270/140	0.1/0.2	1	8

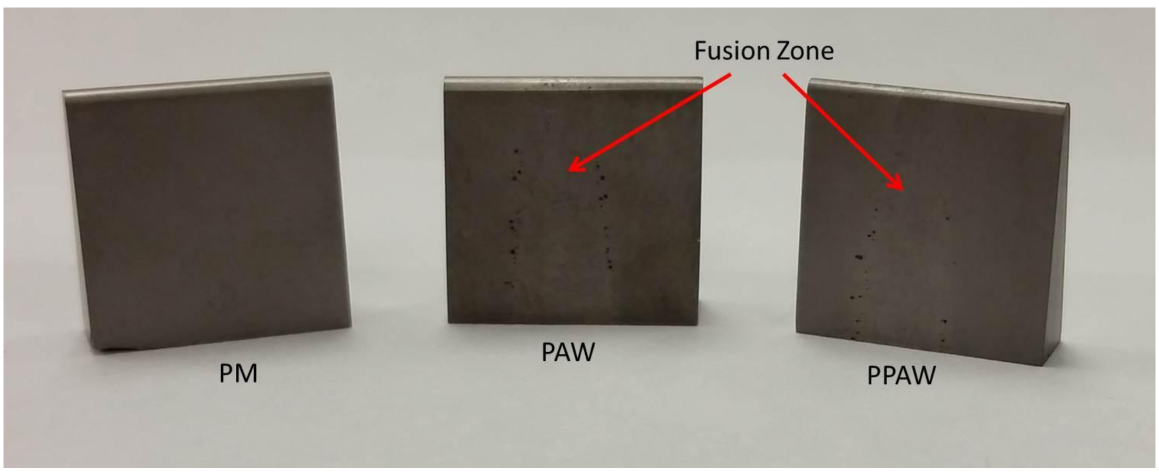

Figure 32: ZrB_2-20ZrC PM, PAW, and PPAW wedges. Nominally 0.5” by 0.5”.

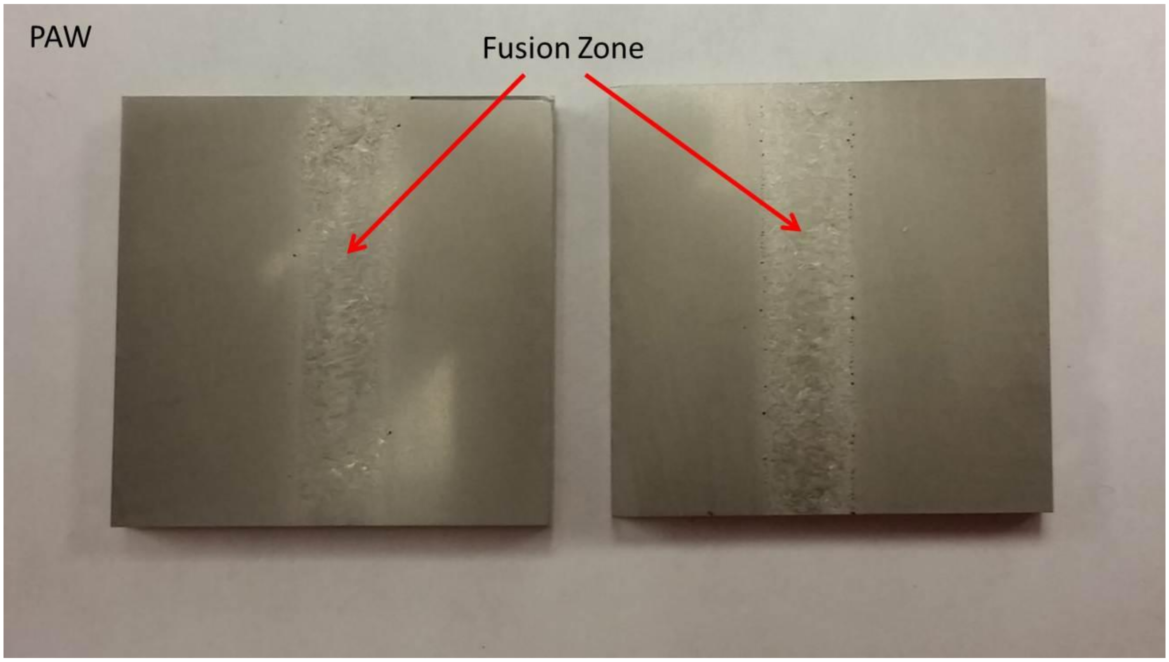

Figure 33: ZrB_2-20ZrC PAW plates, nominally 1" by 1".

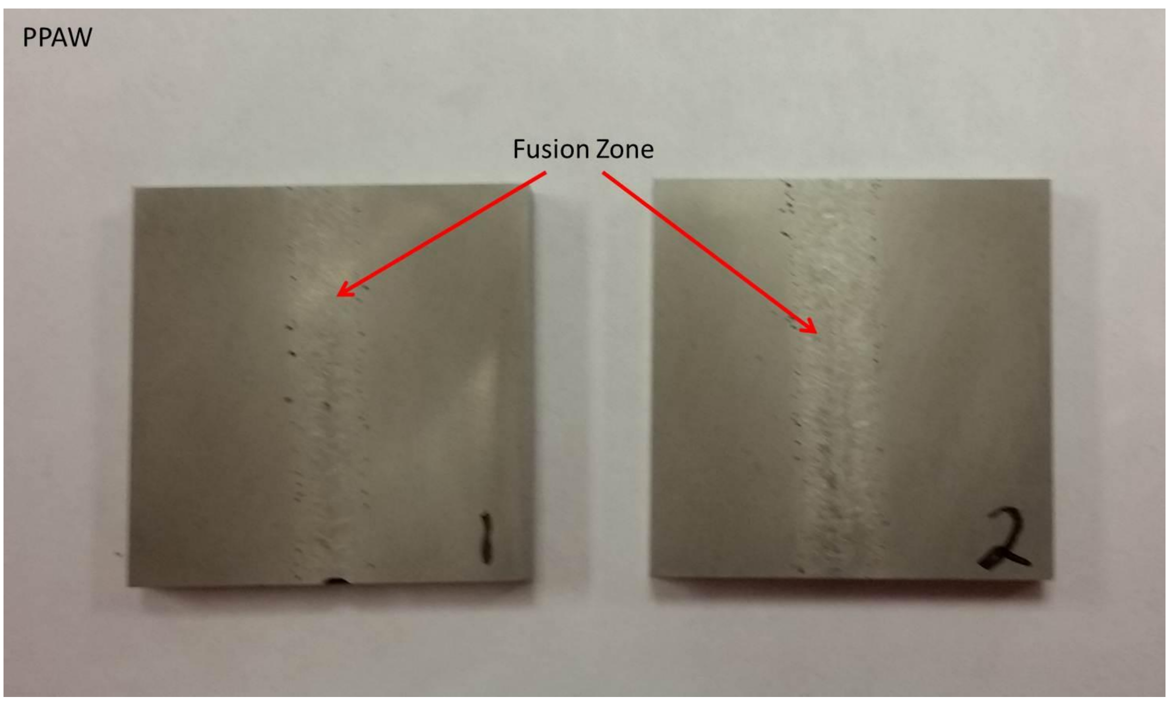

Figure 34: ZrB_2-20ZrC PPAW plates 1 and 2 welded at speeds of 12 and 8 cm/min, respectively. Nominally 1" by 1".

Eight welded ceramic components and four parent material were also submitted to Prof. Douglas Fletcher at the University of Vermont for plasma jet testing. Below is a detailed description of each sample:

4 Parent material (PM) discs

4 Plasma arc welded (PAW) discs

4 Pulsed plasma arc welded (PPAW) discs

The parent material composition was ZrB_2 containing 20 vol% particulate ZrC (ZrB_2-20ZrC). All welded specimens were cut parent material that was welded back together. Before welding, all specimens were pre-heated at a heating rate of 50°C/min to a temperature of 1450°C. After welding, the specimens were held at temperature for ~5 min, and cooled at a rate of 20°C/min to RT. The welding parameters are listed in Table III. PPAW current and pulse times are presented in the format "peak/background". After welding, the specimens were ground flat on top and bottom using a 600 grit diamond machining wheel. Finish grinding of the specimens was performed by hand on a 600 grit polishing pad. Specimen images are included as Figure 35.

Table III: Welding parameters of ZrB_2-20ZrC specimens

Specimen	Welding Current (A)	Pulse Time (s)	Plasma Flow Rate (l/min)	Welding Speed (cm/min)
PAW	180	N/A	0.75	8
PPAW	270/140	0.1/0.2	1	12

Figure 35: ZrB_2-20ZrC PM, PAW, and PPAW discs for testing.

5.0 SUMMARY AND CONCLUSIONS

In summary, the successful fusion welding of UHTCs was demonstrated. The research presented in this report followed the work of a Phase I STTR. At the conclusion of the Phase II STTR, an inert atmosphere chamber was constructed for the welding of UHTCs in a controlled atmosphere. The chamber also housed the necessary equipment to plasma arc weld (PAW) UHTCs. PAW was utilized to weld a variety of UHTCs, and three potential applications were demonstrated that could utilize the fusion welding of UHTCs. Mechanical properties of three different weldments were analyzed and compared to the parent material (PM). Understanding of ZrB_2 solidification and ZrC precipitation within the melt pool was also gained. Below are conclusions of the research presented in this report, which focus on themes of PAW of ZrB_2-

20ZrC, solidification of weld pools, ZrB_2 growth, strength limiting flaws of weldments, and the versatility of PAW.

1. Plasma and pulsed plasma arc welding techniques can be used to fusion weld ZrB_2-20ZrC particulate ceramic composites. Several combinations of current, plasma flow rate, and welding speed can be used to alter the shape of the FZ width and the depth of penetration. For keyhole welds, increased arc power leads to an increase in the size of the weld pool. Increasing current led to larger arc spot sizes.
2. ZrB_2 in the PM had a random orientation and the microstructure of the PM was homogenous. In the FZ, increasing texture occurred with increasing weld pool temperature. In the PM, ZrC was homogenously distributed as a second phase. In the FZ, ZrC was contained in solidified eutectic, or trapped in large ZrB_2 grains, where ZrB_2 grains split and grew around nucleating ZrC.
3. ZrB_2 grew in the melt pool along the basal plane, forming platelet grains. Platelet orientation was determined by the largest thermal gradient acting on growing grains. Platelet thickness increased by ledge growth.
4. Separation of solidifying eutectic from ZrB_2 grains within the plasma arc welded fusion zone resulted in the formation of large voids within the FZ. These voids were determined to be failure origins for plasma arc welded ZrB_2-20ZrC. Void formation was not observed in pulsed plasma arc welded ceramics, but multiple fracture mirrors in a single ZrB_2 grain indicated stress-induced microcracking occurred in pulsed plasma arc welded FZs, leading to failure initiation. When voids were removed from the FZ, the effects of large ZrB_2 grain size controlled the mechanical behavior of the weldments.

5. Plasma arc welding was used to weld both ZrC-20TiC and TiB_2-20TiC ceramics. Porosity was observed in each FZ, indicating the need to refine PM processing and/or welding parameters. Welding of a carbide ceramic also revealed that ceramics with higher electrical resistivities than ZrB_2 can be arc welded, but at this point, the range of electrical resistivities that allow for arc welding is unknown.

The research presented in this report expands the knowledge of ceramic fusion welding and provides a base for future research in this area. Analysis of the effect that welding parameters had on the formation and texture of the FZ, and discussion on the FZ microstructure and how it affects the mechanical properties surpasses that of the previous work on arc welding of ZrB_2 based ceramics. In future studies, control of welding parameters and weld pool temperatures can be used to control the size, solidification behavior, and the resulting microstructure of FZs, leading to desired FZ properties.

Finally, the investigators recommend that research in PAW of ZrB_2-20ZrC ceramics expand upon the parameters of 176 A (current), 1 l/min (plasma flow rate), 12 cm/min (welding speed). This combination of parameters provides sufficient heat to form a FZ, but the increased plasma flow rate will hinder grain growth compared to higher welding currents. To further refine the microstructure, PPAW should be utilized, and an experimental matrix centering around the parameters presented in this research will assist in parameter refinement.

6.0 RECOMMENDATIONS FOR FUTURE WORK

Research presented in this report follows the dissertation work of Dr. Derek S. King (Missouri University of Science and Technology, PhD completed in 2015). This PhD research focused on the fusion welding of ultra-high temperature ceramics, but more work in the area of

ceramic welding in general can be accomplished. Potential future work identified by Dr. King applies to this future work section, with several suggestions for future research that will advance the understanding of the behavior of ceramics during fusion welding.

1. The use of modeling will be useful in understanding the thermal gradients generated during the plasma arc welding process. Information on the temperature of a weld pool, and the thermal gradients surrounding the cooling liquid, can be combined with microstructural observations to describe the nucleation and growth behavior of the diboride in diboride-carbide weld pools. Modeling may then be used to optimize PAW parameters such that the FZ remains at a temperature conducive to high nucleation rates and low growth rates for ceramic grains.
2. It has been observed that a pre-heat is necessary in order to successfully plasma arc weld diboride or carbide based ceramics. Without a pre-heat in excess of ~1300°C, thermal shock of the ceramic has been observed. Therefore, it is suggested that the thermal shock associated with arc welding be investigated.
3. PAW/C-rich FZs were observed to have smaller ZrB_2 grains than PAW or PPAW FZs. It was hypothesized that the introduction of C into the weld pool reduced the temperature of the weld pool as energy was expended during the diffusion of C from the graphite spacer. This occurs as the enthalpy of fusion (ΔH_f) and mixing (ΔH_{mix}) are expected to be positive for the system. In PAW/C-rich welds, the lower temperature of the weld pool promoted nucleation of ZrB_2, but hindered growth. Addition of a filler material with known ΔH_f and ΔH_{mix} can be added to a weld pool during welding, could be used to confirm this hypothesis.

4. Large pores were observed in the FZ of ZrC-20TiC. Porosity was also observed in the HAZ of ZrC-20TiC and ZrB_2-20ZrC weldments. Currently, it is thought that porosity formation occurs due to active oxidation of the non-oxides. X-ray diffraction of the parent material revealed the presence of hongquiite, a cubic TiO, and it is thought that the formation of these pores occurs during oxidation of (Zr,Ti)C with TiO, producing CO/CO_2 gas. It is also known that oxygen impurities exist in the shield and plasma gas. The utilization of pure materials, powders and gasses, may restrict or eliminate pore formation in the FZ and HAZ.
5. The research presented in this dissertation revealed that PAW can be utilized for the fusion joining of ceramics, while previous work on the arc welding of ceramics utilized gas tungsten arc welding (GTAW) processes. Utilizing GTAW, the fusion welding of ceramics containing SiC and B_4C was demonstrated. Attempts at PAW of UHTCs containing SiC and B_4C were not as successful, therefore, it is suggested that the research on fusion welding of ceramics by GTAW be expanded.

7.0 REFERENCES

[1]W. G. Fahrenholtz, G. E. Hilmas, I. G. Talmy, and J. A. Zaykoski, "Refractory Diborides of Zirconium and Hafnium," *J. Am. Ceram. Soc.*, **90**[5] 1347-64 (2007).

[2]E. Rudy and S. Windish, "Ternary Phase Equilibria in Transition Metal-Boron-Carbon-Silicon System: Part V. Compendium of Phase Diagram Data." in**.** Air Force Materials Laboratory, AFML-TR-65-2, Wright Patterson Air Force Base, OH, 1966.

[3]L. Zhang, D. A. Pejaković, J. Marschall, and M. Gasch, "Thermal and Electrical Transport Properties of Spark Plasma-Sintered HfB_2 and ZrB_2 Ceramics," *J. Am. Ceram. Soc.,* **94**[8] 2562-70 (2011).

[4]G.-J. Zhang, Z.-Y. Deng, N. Kondo, J.-F. Yang, and T. Ohji, "Reactive Hot Pressing of ZrB_2–SiC Composites," *J. Am. Ceram. Soc.*, **83**[9] 2330-32 (2000).

[5]D. Sciti, L. Silvestroni, G. Celotti, C. Melandri, and S. Guicciardi, "Sintering and Mechanical Properties of ZrB_2–$TaSi_2$ and HfB_2–$TaSi_2$ Ceramic Composites," *J. Am. Ceram. Soc.,* **91**[10] 3285-91 (2008).

[6]A. L. Chamberlain, W. G. Fahrenholtz, G. E. Hilmas, and D. T. Ellerby, "High-Strength Zirconium Diboride-Based Ceramics," *J. Am. Ceram. Soc.*, **87**[6] 1170-72 (2004).

[7]M. Singh and R. Asthana, "Joining and integration of ZrB_2-based ultra-high temperature ceramic composites using advanced brazing technology," *J. Mater. Sci.*, **45**[16] 4308-20 (2010).

[8]W. R. Pinc, M. Di Prima, L. S. Walker, Z. N. Wing, and E. L. Corral, "Spark Plasma Joining of ZrB_2–SiC Composites Using Zirconium–Boron Reactive Filler Layers," *J. Am. Ceram. Soc.*, **94**[11] 3825-32 (2011).

[9]R. Asthana, M. Singh, and N. Sobczak, "Wetting behavior and interfacial microstructure of palladium- and silver-based braze alloys with C–C and SiC–SiC composites," *J. Mater. Sci.*, **45**[16] 4276-90 (2010).

[10]R. W. Rice, "Joining of Ceramics,*"* pp. 69-111 in Advances in joining technology: proceeding of the 4th Army Materials Technology Conference, Boston, MA, 1976.

[11]G. E. Hilmas, W. G. Fahrenholtz, J. L. Watts, and H. J. Brown-Shaklee, "Ceramic welds, and a method for producing the same,*"* U.S. Patent 8,715,803, (2014).

[12]ASTM (ASTM International), "Dynamic Young's Modulus, Shear Modulus, and Poisson's Ratio for Advanced Ceramics by Impulse Excitation of Vibration", ASTM Standard C1259-08E1, West Conshohocken, PA., (2008).

[13]ASTM (ASTM International), "Standard Test Methods for Determination of Fracture Toughness of Advanced Ceramics at Ambient Temperature", ASTM Standard C1421-10, West Conshohocken, PA., (2010).

[14]ASTM International (ASTM), "Standard Test Method for Flexural Strength of Advanced Ceramics at Ambient Temperature", ASTM Standard C1161-02c, West Conshohocken, PA., (2008).

[15]C. S. Wu, C. B. Jia, and M. A. Chen, "A Control System for Keyhole Plasma Arc Welding of Stainless Steel Plates with Medium Thickness," *Supplement to the Welding Journal,* **89** 225-31 (2010).

[16]Z. Liu, C. S. Wu, and J. Gao, "Vision-based observation of keyhole geometry in plasma arc welding," *International Journal of Thermal Sciences,* **63**[0] 38-45 (2013).

[17]H. G. Fan and R. Kovacevic, "Keyhole formation and collapse in plasma arc welding," *J. Phys. D: Appl. Phys.*, **32**[22] 2902-09 (1999).

[18]Z. M. Liu, C. S. Wu, and M. A. Chen, "Visualizing the influence of the process parameters on the keyhole dimensions in plasma arc welding," *Meas. Sci. Technol.*, **23**[10] (2012).
[19]Y. M. Zhang and S. B. Zhang, "Observation of the keyhole during plasma arc welding," *Welding Journal*, **78**[2] 53s-58s (1999).
[20]E. S. Machlin, pp. 263-88. in An Introduction to Aspects of Themodynamics and Kinetics Relevant to Materials Science**.** Elsevier, Oxford, UK, 2007.
[21]D. S. King, G. E. Hilmas, and W. G. Fahrenholtz, "Plasma Arc Welding of TiB_2-20 vol.% TiC," *J. Am. Ceram. Soc.*, **97**[1] 56-59 (2014).
[22]T. Zhang, C. S. We, and Y. Feng, "Numerical Analysis of Heat Transfer and Fluid Flow in Keyhole Plasma Arc Welding," *International Journal of Computation and Methodology*, **60**[8] 685-98 (2011).
[23]P. V. Huong, "Structural studies of diamond films and ultrahard materials by Raman and micro-Raman spectroscopies," *Diamond Relat. Mater.*, **1**[1] 33-41 (1991).
[24]D. S. King, G. E. Hilmas, and W. G. Fahrenholtz, "Plasma arc welding of ZrB_2-20 vol% ZrC ceramics," *J. Eur. Ceram. Soc.*, **34**[15] 3549-57 (2014).
[25]N. L. Okamoto, M. Kusakari, K. Tanaka, H. Inui, and S. Otani, "Anisotropic elastic constants and thermal expansivities in monocrystal CrB_2, TiB_2, and ZrB_2," *Acta Mater.*, **58**[1] 76-84 (2010).
[26]K. K. Chawla, "Composite Materials: Science and Engineering," Second ed. Springer: New York, NY, (1998).
[27]G. E. Hilmas, D. R. Beeaff, A. C. Mulligan, M. M. Opeka, M. J. Rigali, and M. P. Sutaria, "Forming feed rod comprising a thermoplastic polymer and ceramic or metallic particulate material; forming hole in rod; inserting start of continuous spool of ceramic fiber, metal fiber, or carbon fiber; extruding to form continuous filament," U.S. Patent 6,355,338, (2002).
[28]G. T. Colwell and J. M. Modlin, "Heat pipe and surface mass transfer cooling of hypersonic vehicle structures," *J. Thermophys. Heat Transfer*, **6**[3] 492-99 (1992).
[29]J. M. Modlin and G. T. Colwell, "Surface cooling of scramjet engine inlets using heat pipe, transpiration, and film cooling," *J. Thermophys. Heat Transfer*, **6**[3] 500-04 (1992).
[30]T. Tsuchida and S. Yamamoto, "Spark plasma sintering of ZrB_2–ZrC powder mixtures synthesized by MA-SHS in air," *J. Mater. Sci.*, **42**[3] 772-78 (2007).
[31]R. Chang and L. J. Graham, "Low Temperature Elastic Properties of ZrC and TiC," *J. Appl. Phys.*, **37**[10] 3778-83 (1966).
[32]L. Silvestroni and D. Sciti, "Oxidation of ZrB_2 Ceramics Containing SiC as Particles, Whiskers, or Short Fibers," *J. Am. Ceram. Soc.*, **94**[9] 2796-99 (2011).
[33]E. W. Neuman, G. E. Hilmas, and W. G. Fahrenholtz, "Strength of Zirconium Diboride to 2300°C," *J. Am. Ceram. Soc.*, **96**[1] 47-50 (2013).
[34]E. Kang and C. Kim, "Improvements in mechanical properties of TiB_2 by the dispersion of B_4C particles," *J. Mater. Sci.*, **25**[1] 580-84 (1990).
[35]S. H. Shim, K. Niihara, K. H. Auh, and K. B. Shim, "Crystallographic orientation of ZrB_2-ZrC composites manufactured by the spark plasma sintering method," *Journal of Microscopy*, **205**[3] 238-44 (2002).
[36]J. B. Wachtman, W. R. Cannon, and M. J. Matthewson, "Mechanical Properties of Ceramics," 2nd ed. John Wiley & Sons, Inc.: Hoboken, NJ, (2009).

[37] J. J. Meléndez-Martínez, A. Domínguez-Rodríguez, F. Monteverde, C. Melandri, and G. de Portu, "Characterisation and high temperature mechanical properties of zirconium boride-based materials," *J. Eur. Ceram. Soc.,* **22**[14–15] 2543-49 (2002).
[38] J. J. Cleveland and R. C. Bradt, "Grain Size/Microcracking Relations for Pseudobrookite Oxides," *J. Am. Ceram. Soc.,* **61**[11-12] 478-81 (1978).
[39] J. Watts, G. Hilmas, and W. G. Fahrenholtz, "Mechanical Characterization of ZrB_2–SiC Composites with Varying SiC Particle Sizes," *J. Am. Ceram. Soc.,* **94**[12] 4410-18 (2011).

APPENDIX A-Personnel and Publications

Personnel

Dr. Cheol-Woon (CW) Kim - Principal Investigator, MO-SCI Corporation

Joe Szabo - Research Engineer, MO-SCI Corporation

Ray Crouch - Research Technician, MO-SCI Corporation

Prof. Gregory E. Hilmas - Co-Principal Investigator, Missouri S&T

Prof. William G. Fahrenholtz - Co-Principal Investigator, Missouri S&T

Derek S. King – PhD Graduate Student, Missouri S&T

Andrew Schlup – Undergraduate Student, Missouri S&T

Carolina (Cari) Swanson – Undergraduate Student, Missouri S&T

Publications

1. D.S. King, G.E. Hilmas, and W.G. Fahrenholtz, "Plasma Arc Welding of TiB_2-20 vol% TiC," *Journal of the American Ceramic Society*, 97[1] 56-59 (2014).

2. D.S. King, G.E. Hilmas, and W.G. Fahrenholtz, "Plasma Arc Welding of ZrB_2-20 vol% ZrC Ceramics," *Journal of the European Ceramic Society*, 34[15] 3549-57 (2014).

3. D.S. King, G.E. Hilmas, and W.G. Fahrenholtz, "Corrigendum to Plasma Arc Welding of ZrB_2-20 vol% ZrC Ceramics," *Journal of the European Ceramic Society*, 35[5] 1657 (2015).

4. D.S. King, G.E. Hilmas, and W.G. Fahrenholtz, "Mechanical Behavior and Applications of Arc Welded Ceramics," *International Journal of Applied Ceramic Technology*, Accepted for publication (to be published in 2015).

APPENDIX B-Presentations/Posters and Abstracts

Titles and Abstracts are listed below, by year, for several presentations based on the work funded by this Phase II STTR project. The presenter of each presentation was the first author, unless otherwise specified. A total of 7 oral presentations and 4 posters were presented. It is important to note that due to the early submission deadlines for conference abstracts, submitted abstracts do not always represent the data and discussion of the presentation.

2013

International Conference on Advanced Ceramics and Composites (ICACC)

Welding of Ultra High Temperature ZrB_2 Ceramics (Contributed Oral Presentation)

Authors: Derek King, Greg E. Hilmas, and William G. Fahrenholtz

Plasma arc welding was used to join zirconium diboride (ZrB_2) based ceramics. ZrB_2 billets were prepared by milling ZrB_2 powder in acetone with phenolic resin as a sintering aid and hot-pressing at temperatures up to 2200°C to achieve near theoretical densities. Billets nominally 64 mm by 64 mm by 5 mm were ground and diced using an automated surface grinder. Diced pieces were welded together using an in-house plasma arc welding process. To combat oxidation and thermal shock, welding was carried out under an inert argon atmosphere in a sealed furnace designed to preheat the samples prior to welding. The effectiveness of welding parameters was examined through microstructural analysis of weld cross-sections using scanning electron microscopy. Void formation was also examined with the use of microstructural analysis and density measurements. Elastic constants for melt solidified ZrB_2 were measured using dynamic impulse excitation techniques to determine the Young's modulus for the joint. To test the strength of the joint, flexure bars were prepared so that the weld joint was under maximum load during four-point bend testing.

Pacific Rim Conference of Ceramic Societies (PACRIM)

Plasma Arc Welding of Diboride Ceramics (Contributed Oral Presentation)

Authors: Derek King, Greg E. Hilmas, and William G. Fahrenholtz

Autogenous plasma arc fusion welding was used to join diboride based ceramics. Billets of diborides such as ZrB_2, TiB_2, and HfB_2 were fabricated and machined into smaller pieces. Diced pieces were welded together using an in-house plasma arc welding process. To combat oxidation and thermal shock, welding was carried out under an inert argon atmosphere in a sealed furnace designed to preheat the samples prior to welding. Weld cross-sections were examined to determine the melt efficiency of the weld based on power input and weld speed. Scanning electron microscopy was used to study how the microstructure of a melt solidified diboride differed from a hot-pressed or pressurelessly sintered materials. X-ray diffraction was also used to determine whether melt cooling had any effect on the crystallographic nature of the diborides. Four-point flexure testing was used in determining joint strength with maximum load on the joint, while elastic constants were measured using dynamic impulse techniques.

Materials Science and Technology (MST)

Welding of Diboride-Based Ultra-High Temperature Ceramics (Contributed Oral Presentation)

Authors: Derek King, Greg E. Hilmas, William G. Fahrenholtz, and Cheol-Woon Kim

Diborides such as ZrB_2 and TiB_2, as well as diboride-carbides such as ZrB_2-ZrC and TiB_2-TiC, were fabricated and machined to produce tests specimens designed to be edge welded to produce a monolithic, welded ceramic. Autogenous welding was performed using a plasma arc welding process under an argon atmosphere to limit oxidation. A custom graphite element furnace was used to preheat the samples to ~1450^{o}C prior to welding, to avoid thermal shock. Currents ranging from 130 to 200 A, plasma flow rates of 0.75 and 1.00 l/min., and a welding speed of ~2

cm/min. were used for welding. Microstructural analysis of weld pools was carried out using optical microscopy, scanning electron microscopy, and X-ray diffraction for comparison to the parent materials. Elastic constants and density measurements were used for flaw detection such as porosity and microcracking. Four-point flexure testing was used to determine joint strength with maximum load on the joint.

Aerospace Materials for Extreme Environments Program Review

Welding of ZrB_2-Based Ultra-High Temperature Ceramics

Authors: Cheol-Woon Kim, Greg E. Hilmas, and William G. Fahrenholtz

<u>2014</u>

ICACC

Mechanical Properties of Fusion Welded ZrB_2 containing 20 vol.% ZrC (Invited Oral Presentation)

Authors: Derek King, Greg E. Hilmas, and William G. Fahrenholtz

Plasma arc welding was used to join ZrB_2 containing 20 vol.% ZrC (ZrB_2-20ZrC). The billets were prepared by ball milling ZrB_2 and ZrC powders in acetone with phenolic resin as a sintering aid. Billets nominally 64 mm by 64 mm by 5 mm were hot pressed to near theoretical density, ground to a thickness of 4 mm, and then sliced in half with a diamond saw using an automated surface grinder. The cut halves were fusion welded using a plasma arc welder. To combat oxidation and thermal shock, welding was carried out under an inert argon atmosphere in a sealed furnace designed to preheat the samples prior to welding. The strengths of the joints were compared to that of the parent material following the guidelines of ASTM C1469-10. Hardness was also used to determine if a heat affected zone was apparent in the joint. Scanning electron

microscopy and x-ray diffraction were used to evaluate the microstructure and composition of the fusion zone.

ICACC

Optimization of Fusion Welding Parameters for ZrB_2-20vol.% ZrC (Contributed Poster Presentation)

Authors: Derek King, Greg E. Hilmas, and William G. Fahrenholtz

Plasma arc welding was used to join ZrB_2 containing 20 vol.% ZrC (ZrB_2-20ZrC). The billets were prepared by ball milling ZrB2 and ZrC powders in acetone with phenolic resin as a sintering aid. Billets nominally 64 mm by 64 mm by 5 mm were hot-pressed to near theoretical density, diamond machined, and diced into coupons. Welding current, plasma flow rate, and welding speed were optimized using a 3^3 factorial experiment. Completed welds were evaluated for penetration depth and porosity, and assigned a figure of merit to determine effectiveness of the parameter combination. Pre-heats of the coupons, prior to welding, were used to aid in the resistance to thermal shock. In order to reduce pre-heat temperatures, parameters from the 3^3 factorial that produced effective welds were then subjected to a 2^3 factorial in which current ramp rate and temperature were studied. Hardness and penetration measurements were used to determine the effectiveness of the current ramp rate and pre-heat combinations in order to optimize the welding parameters of ZrB_2-20ZrC based on welding current, plasma flow rate, welding speed, current ramp rate, and pre-heat temperature.

Materials Challenges in Alternative and Renewable Energy (MCARE)

Plasma Arc Welding of ZrB_2 20 vol.% ZrC and $Zr^{11}B_2$ (Contributed Oral Presentation)

Authors: Derek King, Jason Lonergan, Greg E. Hilmas, and William G. Fahrenholtz

Plasma arc welding was used to join coupons of ZrB_2 containing 20 vol.% ZrC (ZrB_2-20ZrC), and melt $Zr^{11}B_2$ specimens. ZrB_2-20ZrC powders were hot-pressed to produce dense billets at a temperature of 1980°C with phenolic resin as a sintering aid. $Zr^{11}B_2$ billets were formed using reaction hot-pressing of ZrH_2 and ^{11}B powders at a temperature of 2100°C. To combat oxidation and thermal shock, welding was carried out under an inert argon atmosphere in a sealed furnace designed to preheat the samples prior to welding. Melt pools from the $Zr^{11}B_2$ specimens were analyzed using SIMS to determine isotope ratios before and after melting. Thermal diffusivity of the samples was measured from room temperature to 2000°C and was used to calculated thermal conductivities for both ZrB_2-20ZrC and $Zr^{11}B_2$. At room temperature, thermal conductivities of 68 and 137 W/mK were measured for ZrB_2-20ZrC and $Zr^{11}B_2$, while thermal conductivity was seen to drop to 62 and 84 W/mK at 2000°C. With a high thermal conductivity, strengths reported to be ~220 MPa at temperatures above 1600°C, and the ability to be arc welded (with additions of ZrC), ZrB_2 may be a versatile material for cladding applications in nuclear reactors.

Chancellors Fellowship Poster Presentation

Flexure Strength Analysis of Arc Welded ZrB_2-20vol.% ZrC

Authors: Derek King, Greg E. Hilmas, and William G. Fahrenholtz

Materials Science and Engineering Seminar

Flexure Strength Analysis of Arc Welded ZrB_2-20vol.% ZrC (Oral Presentation)

Authors: Derek King, Greg E. Hilmas, and William G. Fahrenholtz

Zirconium diboride (ZrB_2) and zirconium carbide belong to the class of ultra high temperature ceramics (UHTCs) due to their high melting temperature, >3000°C. The general public thinks of

ceramics as sinks, tiles, or plates. Further, ask the average non-materials engineer to describe a ceramic and they would likely describe them as “big, white thermal and electrical insulators”. The field of ceramic engineering is much larger, and the purpose of this research is to demonstrate the ability to arc weld ceramics. At room temp, ZrB_2 exhibits a low electrical resistivity (8 $\mu\Omega\cdot$cm) and a high thermal conductivity (>130 W/m·K), similar to metals, however, the mechanical properties of ZrB_2 are synonymous with ceramic mechanical behavior, i.e., brittle. Therefore, 20 vol% ZrC is added to ZrB_2 (ZrB_2-20ZrC) to decrease the melting temperature and improve the mechanical properties of ZrB_2 during the arc welding process. ZrB_2-20ZrC ceramic billets were densified, through the application of high heat and pressure, and sectioned to produces coupons for welding. Plasma arc welding was used to weld the coupons back together in an inert argon atmosphere in a sealed furnace designed to preheat the samples prior to welding. The microstructure of the fusion zones were characterized to understand solidification while characterization of strength was used to determine the effect that fusion welding has on the mechanical properties of ZrB_2-20ZrC.

Counsel of Graduate Students Poster Presentation

Analysis of Arc Welded Zirconium Diboride Ceramics

Authors: Derek King, Greg E. Hilmas, and William G. Fahrenholtz

National Space and Missile Materials Symposium (NSMMS)

Arc Welded ZrB_2 Based Ceramics and Their Flexure Strengths (Contributed Oral Presentation)

Authors: Derek King, Greg Hilmas, and William G. Fahrenholtz

Plasma arc welding was used to join ZrB_2 based ceramics containing various amounts of ZrC and ZrO_2 as secondary phases. The billets were prepared by ball milling zirconium based

ceramic powders in acetone with ZrB_2 media, to achieve good mechanical mixing. Billets nominally 45 mm by 32 mm by 5 mm were hot pressed to near theoretical density at 1980°C, ground to a thickness of 4 mm, and then sliced in half with a diamond saw using an automated surface grinder. The cut halves were autogenously fusion welded using a plasma arc welder. To combat oxidation and thermal shock, welding was carried out under an inert argon atmosphere in a sealed furnace designed to preheat the samples prior to welding. Pre-heat temperatures between 1250 and 1700°C were utilized. The flexure strengths of the joints were characterized in 4 pt. bending and compared to that of the parent material, following the guidelines of ASTM C1161. Scanning electron microscopy and x-ray diffraction were used to evaluate the microstructure and composition of the fusion zone. Hardness was also used to determine if a heat affected zone was apparent in the weldment. The ability to produce complex shapes through arc welding diboride based ceramics is shown through the development of a leading edge.

Materials Science and Technology (MST)

Grain Growth of ZrB_2 in Pulse Plasma Arc Welded Fusion Zones (Undergraduate Poster Competition)

Authors: Cari Swanson, Derek King, Greg Hilmas, Bill Fahrenholtz

Pulse plasma arc welding (PPAW) was used to join ZrB_2 based ceramics. ZrB_2 containing 25 vol% ZrC and 10 vol% WC was densified by hot pressing at 1980°C under argon. Machined coupons, nominally 31 mm by 11 mm by 4 mm, were welded in an inert argon environment to reduce oxidation and preheated to 1450°C to reduce thermal shock. Welds were cross-sectioned and analyzed using optical microscopy. The largest ZrB_2 grains grew to lengths that ranged from

2.3 mm to 0.4 mm for different fusion zones. PPAW parameters were refined to affect the growth of ZrB_2 in ceramic fusion zones.

Aerospace Materials for Extreme Environments Program Review

Welding of ZrB_2-Based Ultra-High Temperature Ceramics

Authors: Cheol-Woon Kim, Greg E. Hilmas, and William G. Fahrenholtz

2015

ICACC

Modeling of Fusion Zone Temperatures in ZrB_2-ZrC Ceramic Weld Pools (Contributed Oral Presentation)

Authors: Derek King, Greg E. Hilmas, and William G. Fahrenholtz

Presenter: Jeremy Watts

Plasma arc welding has been used to join ZrB_2 containing 20 vol.% ZrC (ZrB_2-20ZrC). The resulting fusion zones exhibit exaggerated growth of ZrB_2, which can limit the mechanical properties of the welded ceramic. Therefore, there is a need to understand the grain growth and nucleation kinetics of the ceramic crystals that are forming in the fusion zone. Taking the power input from welding into consideration, the thermal gradients and temperatures within the fusion zone can be modeled. An IR camera was used to monitor the welding process where pixel brightness was correlated to the temperatures produced during welding. The measured temperatures were then compared with the predicted temperatures from the model. An accurate model for predicting temperature can then be applied for a better understanding of grain growth and nucleation kinetics. The presentation will discuss development of the model and implementation such that during welding the weld pool temperature allows for high nucleation rates while limiting growth of ZrB_2.

LIST OF ACRONYMS AND DESIGNATIONS

Acronyms

UHTC-Ultra High Temperature Ceramic

PAW-Plasma Arc Welding

PPAW-Pulsed Plasma Arc Welding

GTAW-Gas Tungsten Arc Welding

TIG-Tungsten Inert Gas

PM-Parent Material

HAZ-Heat Affected Zone

FZ-Fusion Zone

SEM-Scanning Electron Microscopy

EBSD-Electron Backscatter Diffraction

XRD-X-ray Diffraction

Material Designations

ZrB_2-Zirconium diboride

ZrC-Zirconium carbide

TiB_2-Titanium diboride

TiC-Titanium carbide

C-Carbon

SiC-Silicon carbide

B_4C-Boron carbide

W-Tungsten

WC-Tungsten carbide

ZrB_2-20ZrC-ZrB_2 containing 20 vol% ZrC

TiB_2-20TiC-TiB_2 containing 20 vol% TiC